RSC Advances

PAPER

View Article Online
View Journal | View Issue

Cite this: *RSC Adv.*, 2024, **14**, 40198

Exploring the role of *Chrysanthemum coronarium* leaves distillation waste as a green inhibitor for carbon steel in acidic environment: an integrated study†

Rachid Kellal, [a] Mustapha Zertoubi, [a] Zaki S. Safi, [b] Nuha A. Wazzan, [c] Ohoud S. Al-qurashi[d] and Driss Benmessaoud Left *[a]

In this study, the assessment of the *Chrysanthemum coronarium* leaves' co-product resulting from the hydrodistillation process was conducted to evaluate its anticorrosive potential for carbon steel in the hydrochloric acid medium. Phytochemical analysis of this biomass revealed its abundance in terms of polyphenols and flavonoids; hence the determination of total polyphenol content recorded a value of 75.4 mg GAE per g extract. This was corroborated by FTIR spectroscopy, which revealed the presence of various functional groups, thereby providing positive indications regarding the anticorrosive properties of this plant material. Electrochemical impedance spectroscopy and Tafel extrapolation analysis of polarization curves indicated that the extract from *Chrysanthemum coronarium* leaves reduced the corrosion rate of steel in 1 M HCl medium, reaching 78% in corrosion inhibition efficiency while following an adsorption process governed by the Langmuir isotherm. Furthermore, temperature effect investigations at a range between 293–313 K on the corrosion rate of carbon steel in the acidic medium in the presence and absence of CCLE revealed that the latter undergoes chemisorption-type adsorption on the active metal surface, thereby minimizing its degradation rate at elevated temperatures. The synergistic effect between the *Chrysanthemum coronarium* leaf extract and potassium iodide was examined using both electrochemical techniques, thus reflecting the cooperative abilities of the two compounds in inhibiting carbon steel corrosion. Additionally, scanning electron microscopy images of the surface state confirmed these findings, thereby providing significant insight into the anticorrosive properties of this plant material in corrosive environments. Similarly, a theoretical study using DFT and MD for the major compounds of CCLE confirmed the obtained results, concluding that the plant material derived from the hydrodistillation process of *Chrysanthemum coronarium* leaves exhibits remarkable corrosion inhibition capacity for carbon steel in acidic environments.

Received 16th October 2024
Accepted 28th November 2024

DOI: 10.1039/d4ra07430k

rsc.li/rsc-advances

1 Introduction

Ensuring the seamless and dependable functioning of equipment and products under severe corrosive conditions is fundamental for sustaining efficient technological processes across various industries, both domestically and globally. This challenge has garnered escalating significance, driven by the ever-evolving demands of modern industrial operations. As highlighted by Global Industry Analysts, Inc. (2021), the trajectory of the market demand for products that inhibit corrosion is marked by a robust upward trend, poised for significant expansion. Projections indicate an impressive compounded annual growth rate of the corrosion monitoring market size at a CAGR of 8.5% during the forecast period 2021–2026, with anticipated market valuation soaring to a substantial $3.1 billion by 2026.[1] This growth underscores the critical role that corrosion protection plays in safeguarding assets, enhancing operational reliability, and sustaining industrial productivity in the face of corrosive challenges. Across various industries, a plethora of corrosion regulations have been implemented to address the pervasive concern of metal deterioration for both existing and prospective assets.[2] Amid these diverse approaches, the exploitation of organic corrosion inhibitors appears as a significant approach for corrosion

[a]*Laboratory Interface Materials Environment (LIME), Faculty of Sciences Ain Chock, Hassan II University of Casablanca, B.P 5366, Morocco. E-mail: benmessaoudleftdriss@gmail.com*

[b]*Al Azhar University-Gaza, Chemistry Department, Faculty of Science, P. O. Box 1277, Gaza, Palestine*

[c]*King Abdulaziz University, Chemistry Department, Faculty of Science, P. O. Box 42805, Jeddah, 21589, Saudi Arabia*

[d]*University of Jeddah, Chemistry Department, Faculty of Science, Jeddah, Saudi Arabia*

† Electronic supplementary information (ESI) available. See DOI: https://doi.org/10.1039/d4ra07430k

suppression in harsh conditions. To date, corrosion inhibitors have been systematically categorized into three primary classifications: cathodic, anodic, and mixed-type inhibitors. Cathodic inhibitors primarily reduce the cathodic reaction, such as hydrogen evolution or oxygen reduction, by forming a protective barrier or interfering with the reduction process. Anodic inhibitors, on the other hand, suppress the anodic metal dissolution reaction by forming a passivating film over the metal surface. Mixed-type inhibitors simultaneously impact both anodic and cathodic processes, providing balanced protection by minimizing both metal dissolution and reduction reactions.[3] Leveraging their inherent chemical attributes, characterized by the presence of lone non-bonding electron pairs facilitated by nitrogen and oxygen heteroatoms, alongside their propensity to engage with metal surfaces *via* vacant d-orbitals, organic corrosion inhibitors stand as robust tools for mitigating the deleterious effects of harsh environments. Consequently, their application leads to a discernible reduction in the corrosion rates of metals.[4] Nonetheless, notwithstanding their significant inhibitory effect on metal degradation, the overwhelming majority of these inhibitors are comprised of synthesized chemical compounds, posing potential harm to the ecosystem, entailing high expenses, and possibly exerting adverse effects on human health. In response to the pressing environmental concerns associated with traditional corrosion inhibitors, there has been a burgeoning interest in the development of eco-friendly alternatives. Among these alternatives, organic inhibitors derived from natural sources have emerged as promising solutions. A diverse array of environmentally friendly inhibitor categories, including biopolymers,[5] ionic liquids,[6] amino acids,[7] and plant extracts, have garnered significant attention from researchers and practitioners alike. The exploit of plant extracts, in particular, has attracted considerable interest due to several compelling reasons.[8] Plant extracts offer a more accessible and cost-effective solution, in which the extraction procedures of these natural compounds typically require minimal processing and can be achieved using simple techniques, without the need for sophisticated facilities or solvents.[9] Moreover, plant extracts contain a rich array of phytochemicals, including heteroatoms, which confer notable anticorrosion properties. These natural compounds possess inherent electron-donating capabilities, enabling them to form protective layers on metal surfaces and inhibit corrosion processes effectively. Additionally, their biodegradable nature and low environmental impact make them highly attractive for use in various industrial applications.[10–16] However, it is imperative to recognize that certain plant extracts may exhibit modest and erratic corrosion inhibition properties. Consequently, the synergistic pairing of these extracts presents an intriguing avenue for exploration. Particularly noteworthy is the interaction between halide ions such as chloride (Cl^-), bromide (Br^-), or iodide (I^-), and the phytochemical constituents of the plant extract.[17] This interaction has the potential to substantially augment the corrosion inhibition effect of the electrolyte, all while minimizing the need for substantial quantities of the extract.[18] In our investigation, we sought to employ potassium iodide as a synergistic catalyst due to its high synergistic potential when compared to other halide compounds. This advantage arises mostly from its capacity to swiftly generate a dipole moment owing to its greater molecular size.[19] Within the frame of this work, we opted to investigate the corrosion resistance capability of *Chrysanthemum coronarium* leaves through electrochemical assessments. This genus of the Asteraceae botanical family serves multiple purposes, primarily for the food and pharmaceutical sectors.[20] In formulating the methodological framework of this research endeavor, we were particularly intrigued by the prospect of exploiting the liquid waste generated from the hydrodistillation processes commonly employed in numerous cosmetic industries. This byproduct, often deemed undesirable in such industries, harbors a vast reservoir of organic molecules, which we deemed potentially viable as corrosion inhibitors, aligning with our overarching goal of developing cost-effective and environmentally friendly corrosion inhibitors. To elucidate the composition of the green inhibitor, we conducted a comprehensive array of analyses including phytochemical screening, determination of total polyphenol and flavonoid content, and Fourier Transform Infrared (FT-IR) spectroscopy on the aqueous extract of *Chrysanthemum coronarium* leaves. Electrochemical methods of measurement including potentiodynamic polarization as well as electrochemical impedance spectroscopy were applied to assess the inhibitory efficiency towards the carbon steel in a 1 M HCl solution. Carbon steel is widely used in various industries due to its mechanical strength, availability, and cost-effectiveness. However, it is highly susceptible to corrosion in acidic environments, particularly during processes such as acid cleaning, descaling, and acidizing of oil wells. Hydrochloric acid (HCl) is commonly employed in these operations, making it a relevant medium for corrosion studies.[21] The choice of 1 M HCl solution for this study provides a controlled and aggressive environment to evaluate the performance of corrosion inhibitors, mimicking industrial conditions where carbon steel is at significant risk. This allows for an accurate assessment of the inhibitor's efficiency and practical applicability Table 1. Furthermore, we investigated the influence of temperature under identical conditions to ascertain the mechanistic inhibition regime occurring at the metal–solution interface. Furthermore, the synergistic effectiveness of potassium iodide when combined with *Chrysanthemum coronarium* leaves extract (CCLE) in 1 M HCl was assessed, alongside an examination of the surface morphology of carbon steel in the presence and absence of CCLE in the hydrochloric medium. Quantum chemical analyses were also conducted on the primary constituents of the leaf extract identified from existing literature,[22–26] as depicted in Fig. 1.

2 Experimental instruments and methods

2.1 Samples preparation and phytochemical investigations

The leaves of *Chrysanthemum coronarium* sourced from a field in Casablanca, Morocco underwent careful harvesting and immediate washing to ensure cleanliness. A hydrodistillation

Table 1 A contrast of some corrosion inhibitors derived from natural sources according to the literature

Plant name	Substrate	Corrosive medium		Findings: Methods	Findings: IE (%)	Ref.
Peanut shells	Carbon steel	HCl	1 M	PDP/EIS	81%	27
Passiflora edulis sims peel	Mild steel	Simulated circulating cooling water	—	PDP/EIS	85%	28
Ammophila arenaria	Mild steel	HCl	1 M	WL/PDP/EIS	84.32%	29
Thymus vulgaris	304 steel	HCl	1 M	PDP/EIS	62.15%	30
Camellia chrysantha	Q235 steel	HCl	1 M	WL/PDP/EIS	65.13%	31
***Chrysanthemum coronarium* leafs**	**Carbon steel**	**HCl**	**1 M**	**PDP/EIS**	**78%**	**This study**

process using a Clevenger-Apparatus efficiently extracted desired compounds from the leaves. The resulting solid substrate underwent filtration and evaporation before further analysis. Dilutions of *Chrysanthemum coronarium* leaves extract were prepared by adding it to a 1 M HCl solution derived from a stock solution. Various concentrations ranging from 0.1 to 2 mg mL^{-1} were thus obtained. Following a prior study's protocols, phytochemical evaluation, total phenolics, and flavonoid contents analysis (TPC and TFC) were performed on the extract.[17] These analyses unveiled insights into its chemical composition. FT-IR spectroscopy through an IRAffinity-1S spectrophotometer revealed the extract's primary functional groups and aided in understanding its molecular structure.

2.2 Metal characteristics

The investigation involved the analysis of a carbon steel working electrode with the composition containing C values between 0.350 and 0.390, Si at 0.400, Mn ranging from 0.50 to 0.80, S within 0.015–0.035, and a total of Cr + Ni + Mo at 0.63. Before each assessment, the active area underwent meticulous polishing using silicon carbide sheets across 180, 600, and 1200 grades and was subsequently cleaned with distilled water and degreased using acetone.

2.3 Electrochemical measurements

The corrosion behavior of the carbon steel was investigated in this study using electrochemical techniques, in which a PGZ 301 potentiostat–galvanostat controlled by Voltamaster 4 software was operated for the measurements. A typical three-electrode cell configuration was employed, with a rotating carbon steel disk electrode as the working electrode having a surface area of 0.283 cm^2, a platinum rod as the counter electrode, and a saturated Ag/AgCl electrode as the reference. Electrochemical impedance spectroscopy (EIS) assessments were carried out under the natural electrical condition of the steel-solution interface, covering frequencies from 100 kHz to 10 mHz with a voltage magnitude of 10 mV and ten data points per logarithmic decade. Additionally, potentiodynamic polarization (PDP) curves were generated using the same setup, with a scanning rate of 0.5 mV s^{-1} and a potential range of ±200 mV relative to the Open Circuit Potential. To ensure reliability, each experiment was repeated thrice for result averaging and error minimization.

2.4 SEM-EDX analysis

The effect of CCLE on the surface of steel was studied by examining the surface morphology of the steel through the SEM-EDX technique at 293 K using QUATTRO S-FEG-Thermofisher scientific equipment. After immersing the samples in 1 M HCl for 15 hours, they were cleaned thoroughly with deionized water and dried before each SEM-EDX examination.

2.5 DFT details

The inhibitors under study were assessed for potential protonation sites using the Marvin Sketch program.[32] The results indicated that neutral forms predominated at pH = 0.0 (1 M). As a result, the decision was made to examine the anticorrosive impact of the neutral forms of the constituents from *Chrysanthemum coronarium* leaf extract, as illustrated in Fig. 1. The structures of the examined components were constructed and visualized using Gauss View 6.1 software,[33] with all computations conducted using the Gaussian09 suite of programs.[34] The geometries of the neutral forms of the phytochemicals were optimized using the B3LYP method[35–37] in conjunction with the 6-31+g(d,p) basis set. B3LYP has been demonstrated to yield consistent geometries for various systems.[17,38–40] All calculations were performed in an aqueous solution using the Polarized Continuum Model of Solvation (PCM).[41] The optimized geometries were confirmed as energy minima on the potential energy surface (with no imaginary frequencies) through frequency calculations at the optimized geometries using the same level of theory. Additionally, single-point calculations utilizing the Natural Bond Orbital (NBO) analysis code[42] were conducted to determine the Natural Population Analysis (NPA) and the Hirshfeld charges for systems with N, $N+1$, and $N-1$ electrons at the neutral systems' optimized geometries.

The HOMO (E^{inh}_{HOMO}) and LUMO (E^{inh}_{LUMO}) energies were used to calculate the energy gap as their difference ($\Delta E = E^{inh}_{LUMO} - E^{inh}_{HOMO}$), as well as to calculate the metal → inhibitor ($\Delta E_1 = E^{inh}_{LUMO} - E^{Fe}_{HOMO}$) and inhibitor → metal ($\Delta E_2 = E^{Fe}_{LUMO} - E^{inh}_{HOMO}$) interactions. It's recognized that adding or removing an electron affects not only the HOMO or LUMO orbitals but all of them. Therefore, using the ionization potential and electron affinity as the negative eigenvalues of HOMO and LUMO respectively, as proposed by the Kohn–Sham orbital theorem, does not produce satisfactory results.[17,43,44] Instead, the vertical ionization potential ($I_v = E_0^+ - E_0$) and vertical electron affinity

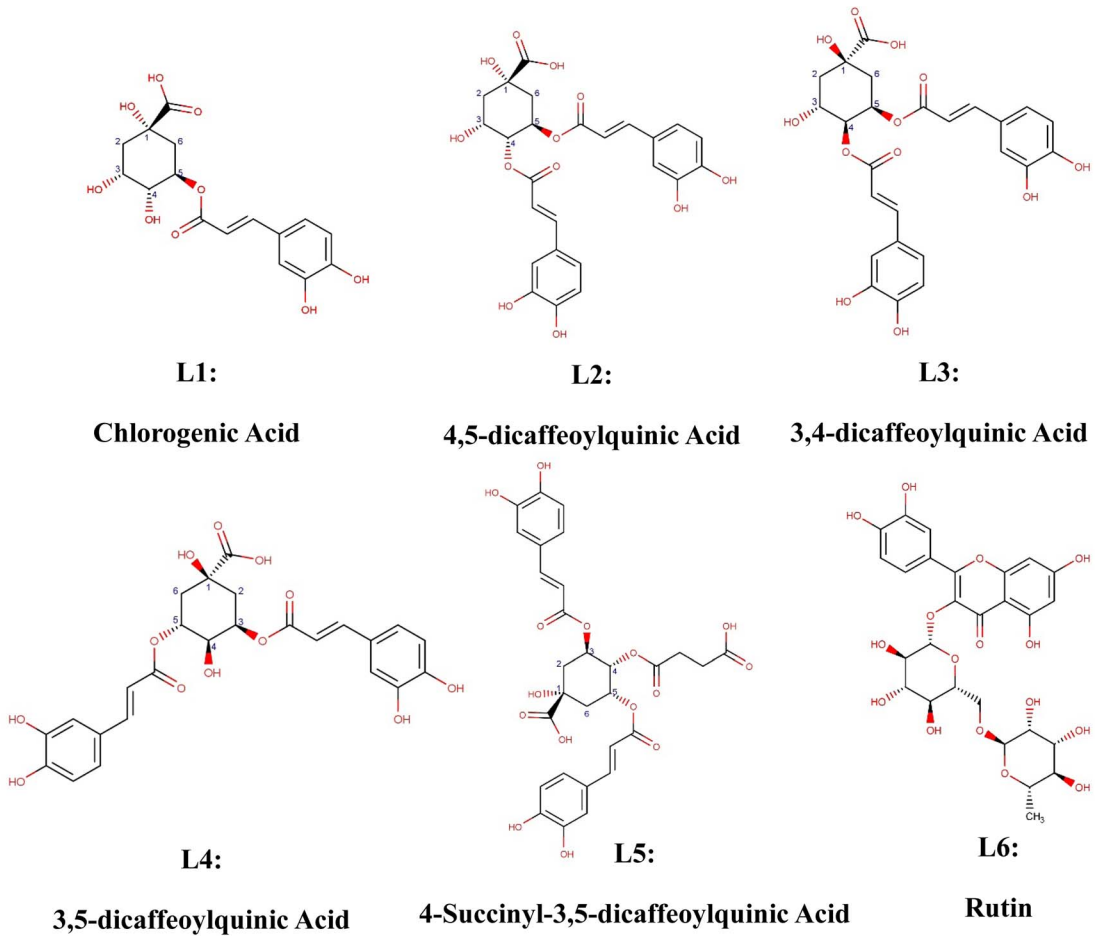

Fig. 1 *Chrysanthemum coronarium* leaves extract major components subjected to investigations.

($A_v = E_0^- - E_0$) were employed to compute global quantum chemical reactivity descriptors. Here, E_0 represents the total energy of the optimized structure for the system with N electrons, while E_0^- and E_0^+ pertain to the energies of the systems with $N-1$ and $N+1$ electrons at the optimal structure of the neutral species with N electrons.

Eqn (1)–(7) were used to calculate the following quantum chemical descriptors.[45] Using the following equations:[38,46–52]

$$\text{Chemical potential}(\mu),\ \text{Electronegativity}(\chi)$$
$$\chi = -\mu = \frac{I_v + A_v}{2} \quad (1)$$

$$\text{Hardness}(\eta) \quad \eta = \frac{I_v - A_v}{2}, \quad (2)$$

$$\text{Softness}(\sigma) \quad \sigma = \frac{1}{\eta} \quad (3)$$

$$\text{Electrophilicity}(\omega) \quad \omega = \frac{\mu^2}{2\eta}, \quad (4)$$

$$\text{Nucleophilicity}(\varepsilon) \quad \varepsilon = \frac{1}{\omega} \quad (5)$$

Electron-donating power (ω^-), electron accepting power (ω^+), net electrophilicity ($\Delta\omega^\pm$)

$$\omega^- = \frac{(3I_v + A_v)^2}{16(I_v - A_v)},$$
$$\omega^+ = \frac{(I_v + 3A_v)^2}{16(I_v - A_v)}, \quad (6)$$
$$\Delta\omega^\pm = \omega^- + \omega^+$$

The charge transfer model for donation and back-donation ($\Delta E_{b\text{-}d}$)

$$\Delta E_{\text{back-donation}} = \Delta E_{b\text{-}d} = -\frac{\eta}{4} \quad (7)$$

2.6 Local chemical reactivity (LCR)

Fukui Functions (FFs) are essential local reactivity parameters that help explain how electrons in a molecule respond to minor perturbations.[49,53,54] These functions are linked to the electron density and provide local reactivity descriptors by approximating the sites responsible for nucleophilic $f^+(r)$, and electrophilic $f^-(r)$ attacks centers over the molecules[54–56] as well as the dual Fukui functions $f^2(r)$.

2.7 Molecular dynamic simulations details

Calculations of the adsorption energies were carried out using DFT by Vienna *Ab initio* Simulation Package (VASP).[55] Generalized gradient-correlated approximation (GGA)/exchange–correlation functionals Perdew–Burke–Ernzerhof (PBE) were employed with a plane-wave cut-off of 400 eV. An iterative self-consistent of 10^{-4} was employed to optimize geometry. The Fe (110) surface was selected for this investigation because, of all the Fe surfaces, it has the lowest energy and the densest structure.[56,57] Fe (110) surface consists of three layers and its supercells are 4 × 5. Monkhorst–Pack 4 × 4 × 1 (ref. 58) and Fermi level smearing of 0.1 eV were selected to find the electronic structures. van der Waals (VDW) forces between Fe atoms and inhibitors have been considered by DFT-D3 model.[59] The calculations were carried out in an aqueous solution using the Poisson–Boltzmann implicit solvation model in VASP-sol.[60] Applying eqn (8), the energy of the adsorption systems has determined:

$$E_{ads} = E_{(inh@Fe)110} - (E_{(inh)} + E_{(Fe110)}) \quad (8)$$

where $E_{(inh@Fe)110}$ is the total energy of the adsorbed inhibitor on Fe, E_{Fe} is the total energy of the Fe clean surface, $E_{(inh)}$ is the total energy of the isolated optimized inhibitor. As well, the charge density differences were calculated using the following equation:

$$\Delta\rho(r) = \Delta\rho_{(inh@Fe)110}(r) - \Delta\rho_{(Fe110)}(r) - \Delta\rho_{(inh)}(r) \quad (9)$$

3 Experimental results

3.1 Total phenolic, flavonoid content, and phytochemical screening

Polyphenols, coumarin, flavonoids, and tannins derivatives, are natural substances produced by plants, playing crucial roles in shielding them from herbivores and diseases. These substances often form the basis of the healing properties of plants, exhibiting multiple properties such as anti-inflammatory, antioxidant, and anticancer properties. The examination of the *Chrysanthemum coronarium* leaf extract revealed a high concentration of these secondary metabolites, as demonstrated by phytochemical screening, as well as total polyphenol (TPC) and total flavonoid (TFC) analyses (Table 2). Notably, the extract displayed increased levels of polyphenols, tannins, flavonoids, and coumarin derivatives, all renowned for their bioactive qualities.[61] The lower concentrations of terpenoids and quinone derivatives in the extract could be attributed to the solvent's affinity for phenolic compounds during the extraction process. These results suggest that the aqueous *Chrysanthemum coronarium* leaf extract shows potential as a corrosion inhibitor under acidic conditions. These active secondary metabolites are likely responsible for the extract's corrosion inhibition properties, warranting further research and development as a corrosion inhibitor.

3.2 IR analysis

The study employed Fourier Transform Infrared (FTIR) spectroscopy to examine the chemical functional groups present in plant substances derived from the leaf waste of *Chrysanthemum coronarium*. He infrared spectra (Fig. 2) displayed distinct absorption peaks, each representing a specific molecular functional group. For example, the peaks at 3442 cm^{-1} and 2939 cm^{-1} indicated the presence of O–H stretching bonds typical of phenolic structures and C–H stretching vibrations characteristic of alkanes, respectively.[62] Additionally, the peak at 1631 cm^{-1} suggested C=O stretching vibrations.[63–66] The peak at 1413 cm^{-1} was linked to the skeletal vibration of C–O–O bonds, while the peaks at 1269 cm^{-1} and 1107 cm^{-1} were attributed to C–O bonds in esters and alcohol derivatives.[67] The FTIR analysis confirmed the presence of phenolic compounds in the aqueous extract of *Chrysanthemum coronarium* leaves, as indicated by the phytochemical analysis. These results further substantiate the presence of complex functional groups in the *Chrysanthemum coronarium* leaf extract, highlighting the potential therapeutic properties of its compounds.

3.3 Electrochemical experiments

The open circuit potential (OCP) plot for carbon steel in 1 M HCl illustrates the temporal variation of potential in the presence of varying concentrations of the CCLE. A noticeable positive shift in the OCP values at higher extract concentrations indicates the development of a protective layer on the metal surface. This shift suggests a reduction in the anodic dissolution of the metal or a suppression of cathodic reactions, thereby enhancing the corrosion resistance of the material. Furthermore, the stabilization of OCP values over time reflects the progressive formation of a stable inhibitor film, which effectively reduces the interaction between the aggressive chloride ions in the acid solution and the steel surface. Conversely, at lower extract concentrations, the OCP exhibits less pronounced positive shifts, signifying a weaker protective effect. This behavior can be attributed to insufficient coverage of the steel surface by the extract molecules, leading to a less effective barrier against corrosion processes. The concentration-dependent trend observed in the OCP profiles highlights the role of the extract

Table 2 Potential chemical classes, TPC, and TFC of CCLE extract[a]

	Polyphenols	Flavonoids	Coumarin	Terpenoids	Tannins	Quinones	TPC (mg GAE per g extract)	TFC (mg QE per g extract)
CCLE	++	+	+	−	+	−	75.4 ± 0.6	13.6 ± 0.3

[a] ++: higher presence, +: moderate presence, −: negative.

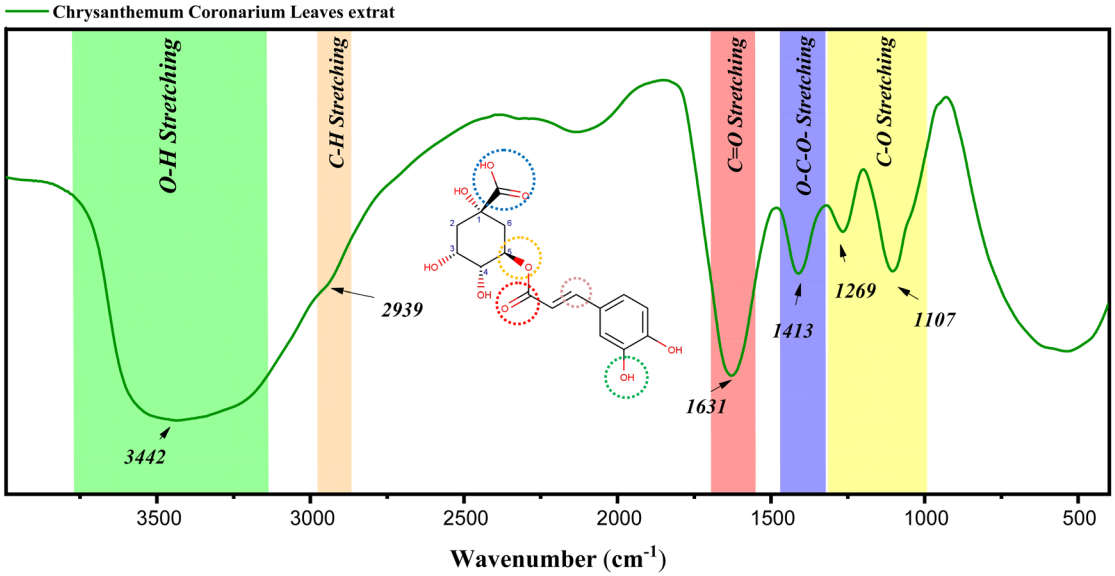

Fig. 2 FTIR spectra of the *Chrysanthemum coronarium* leaf extract through infrared spectroscopy.

concentrations in enhancing inhibition efficiency, with higher concentrations providing more robust protection (Fig. 3).

The meticulous recording of potentiodynamic polarization curves within a 1 M HCl solution, meticulously executed under controlled conditions of temperature (298 K), unveiled intriguing insights into the corrosion behavior of the system under study. The experimental setup encompassed a comprehensive exploration of corrosion dynamics under varying scenarios: in the presence and absence of the CCLE, administered at different concentrations. This systematic investigation aimed to discern the efficacy of the leaf extract as a potential corrosion inhibitor. Fig. 4, a visual rendition of the polarization curves post-extrapolation, serves as a graphical testament to the complex interplay between the corrosive environment and the inhibitive effects exerted by the *Chrysanthemum coronarium* leaf extract.

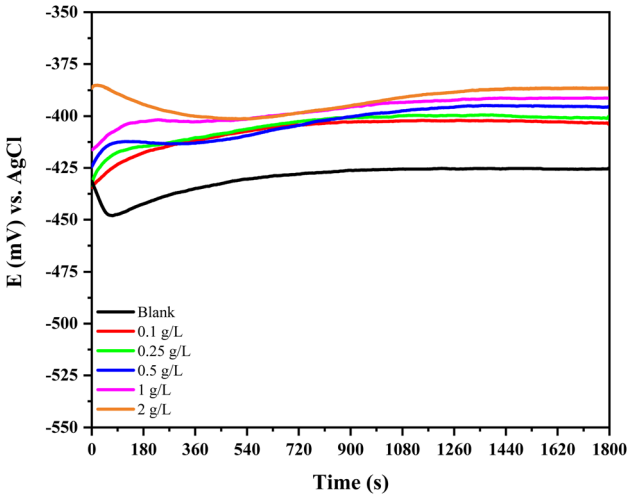

Fig. 3 Open circuit potential (OCP) plots of the carbon steel in the presence of CCLE in 1 M HCl.

Meanwhile, the tabulated data encapsulated in Table 3 provides a quantitative snapshot of the extracted parameters, offering a meticulous breakdown of the corrosion characteristics observed across the experimental spectrum. Analyzing the data reveals a stark contrast between corrosion behaviors in the absence and presence of the leaf extract. Notably, in the absence of the inhibitor, the corrosion current density (i_{corr}) registers a significant value of 0.73 mA cm^{-2}, alongside a corrosion potential (E_{corr}) of −421.37 mV per AgCl, indicative of the aggressive nature of the corrosive medium. However, upon the introduction of varying concentrations of *Chrysanthemum coronarium* leaf extract, a palpable reduction in both cathodic and anodic current densities emerges, underscoring the inhibitive potential of the extract. This inhibitive effect is particularly pronounced even at low concentrations of the extract, as evidenced by the substantial decrease in corrosion current density, reaching a noteworthy low of 0.16 mA cm^{-2} at 2 g L^{-1}, thereby yielding an impressive 78% corrosion inhibition efficiency. Moreover, the observed stability in corrosion potential values across multiple measurements, albeit with subtle deviations towards positive values, hints at the nuanced interplay between the inhibitor and the electrochemical processes governing corrosion kinetics.[68] Of significant interest is the consistency observed in the slopes of both cathodic and anodic Tafel lines (β_c), indicating a parallel increase unaffected by the presence of *Chrysanthemum coronarium* leaf extract. This suggests that the inhibitive action of the extract does not perturb the underlying electrochemical mechanisms transpiring across the anodic and cathodic regions of the C38 steel surface.[69] In essence, this comprehensive analysis underscores the potential of *Chrysanthemum coronarium* leaf extract as an effective corrosion inhibitor in 1 M HCl environment. The extract's ability to mitigate corrosion, even at minimal concentrations, highlights its promising utility in industrial applications aimed at safeguarding metallic structures against corrosive degradation.[70]

Table 3 Tafel characteristics of carbon steel at various concentrations of the CCLE inhibitor

	Concentration (g L^{-1})	E_{corr} *vs.* AgCl (mV)	i_{corr} (mA cm^{-2})	$-\beta_c$ (mV dec^{-1})	β_a (mV dec^{-1})	θ	I.E_{PDP} (%)
CCLE	0	−421.37 ± 0.57	0.73 ± 0.05	119.33 ± 1.20	81.10 ± 1.61	—	—
	0.1	−401.8 ± 3.8	0.38 ± 0.01	133.10 ± 3.89	101.00 ± 8.35	0.493	48
	0.25	−414.3 ± 3.6	0.27 ± 0.01	107.27 ± 3.46	103.20 ± 5.31	0.630	63
	0.5	−396.2 ± 3.2	0.23 ± 0.01	132.77 ± 4.29	87.63 ± 4.71	0.685	68.5
	1	−389.7 ± 2.2	0.18 ± 0.01	120.73 ± 8.21	90.43 ± 7.07	0.753	75.3
	2	−397.2 ± 3.2	0.16 ± 0.01	139.40 ± 8.80	83.6 ± 1.60	0.780	78

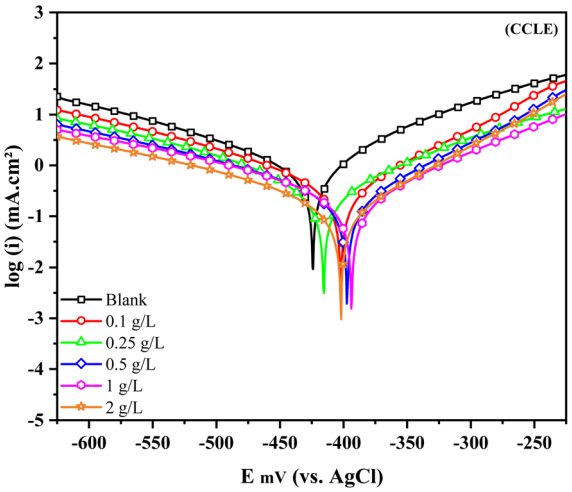

Fig. 4 Tafel plots of the working electrode in the presence of CCLE.

Fig. 5 provides a comprehensive visual representation of Nyquist and Bode diagrams, meticulously generated at the corrosion potential (E_{corr}), offering valuable insights into the corrosion behavior of metallic substrates in the presence of varying concentrations of *Chrysanthemum coronarium* leaf extract (CCLE) at a temperature of 293 K. This analytical approach allows for a nuanced exploration of the electrochemical processes occurring at the metal–solution interface under different inhibitive conditions. The examination of the Nyquist diagrams reveals a consistent capacitive loop for both inhibited and uninhibited metallic samples, positioned beneath the real impedance axis (Z'). This characteristic positioning underscores the predominant role of charge transfer processes in governing the electrochemical corrosion mechanism at play.[13] Such a configuration suggests that the inhibitive action of the *Chrysanthemum coronarium* leaf extract primarily operates through the alteration of charge transfer dynamics, thereby mitigating the corrosion propensity of the metallic substrate. Furthermore, the diameter of the capacitive loop exhibits a notable augmentation with increasing concentrations of the leaf extract within the corrosive medium. This observed trend is corroborated by the data presented in Table 4, which highlights a corresponding rise in polarization resistance, reaching a value of 98.87 Ω cm^2 at a concentration of 2 g L^{-1} of the *Chrysanthemum coronarium* leaf extract. This trend underscores the direct correlation between inhibitor concentration and the impedance of the metallic substrate, implying a more robust inhibitive effect at elevated inhibitor concentrations. Moreover, despite variations in inhibitor concentration, the general morphology of the Bode module curves remains largely invariant. This consistency suggests that the addition of the green inhibitor does not induce significant alterations in the fundamental electrochemical corrosion mechanism governing carbon steel behavior in hydrochloric acid.[71,72] The presence of a singular peak in all Bode phase illustrations further supports this assertion, indicating the presence of a singular time constant characterizing the corrosion process. Additionally, the observed increase in the phase angle peak with escalating inhibitor concentrations signifies an enhancement in capacitive

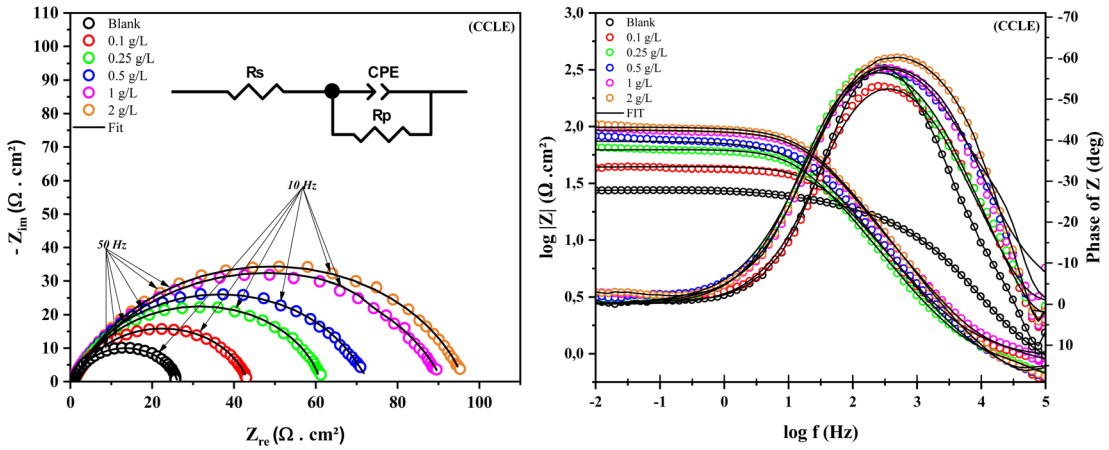

Fig. 5 Nyquist and Bode graphs of the C38 steel in a 1 M HCl solution with different amounts of CCLE introduced.

Table 4 EIS parameters of the carbon steel at various concentrations of the CCLE inhibitor

				CPE				
	Conc. (g L^{-1})	R_s (Ω cm^2)	R_p (Ω cm^2)	Q ($\mu\Omega^{-1}$ s^n cm^{-2})	n	C (μF cm^{-2})	χ^2	I.E_{EIS} (%)
CCLE	0	0.81 ± 0.01	25.47 ± 0.12	424 ± 0.36	0.83 ± 0.01	168	0.002	—
	0.1	0.92 ± 0.17	45.01 ± 2.54	335 ± 0.1	0.79 ± 0.01	109.8	0.001	46
	0.25	1.04 ± 0.44	61.89 ± 1.40	263 ± 0.08	0.79 ± 0.01	88	0.001	59.5
	0.5	0.69 ± 0.03	73.02 ± 1.39	228 ± 0.06	0.79 ± 0.01	76.7	0.001	66.2
	1	0.78 ± 0.19	88.51 ± 1.60	193 ± 0.05	0.78 ± 0.01	61.2	0.001	73.5
	2	0.73 ± 0.01	98.87 ± 6.62	180 ± 0.05	0.78 ± 0.01	57.7	0.001	74.2

behavior at the metal–solution interface. This enhanced capacitive behavior is indicative of greater adsorption of phytochemical compounds from the *Chrysanthemum coronarium* leaf extract onto the metal surface. Consequently, this phenomenon leads to a pronounced attenuation of the electrochemical corrosion process, particularly at higher inhibitor concentrations.

3.4 Temperature effect

Temperature plays a pivotal role in influencing the corrosion mechanisms of metals in harsh environments, affecting the kinetics of corrosion. To assess the corrosion inhibition effectiveness of the *Chrysanthemum coronarium* leaves extract, experiments were conducted across a temperature range from 293 K to 313 K. The optimal concentration of CCLE, set at 2 g L^{-1}, was employed under acidic conditions, using Tafel extrapolation methods. The resulting data, depicted in Fig. 6, illustrate the Tafel diagrams of carbon steel, with and without the inclusion of the green extract, at different temperatures. Remarkably, regardless of the presence of CCLE, the plots display similar shapes, showing an increase in current densities as temperature rises. However, the rate of increase in the inhibited medium appears to be more gradual compared to the uninhibited environment. Table 5 provides a summary of the kinetic parameters obtained from the Tafel extrapolation of the carbon steel electrode. Analysis reveals that increasing temperature leads to higher i_{corr} values in both inhibited and uninhibited media, resulting in progressively reduced inhibitory efficiency. These observations suggest that elevated temperature promotes the adsorption of CCLE molecules from the steel surface, exposing it to corrosive agents and accelerating the corrosion rate.[73] To gain deeper insights into the inhibitory process occurring at the surface interface, investigations into the activation thermodynamics parameters were conducted following established Arrhenius laws:[74]

$$i_{corr} = A \times \exp\left(\frac{-E_a}{R \times T}\right) \quad (10)$$

$$i_{corr} = \frac{R \times T}{N \times h}\exp\left(\frac{\Delta S_a}{R}\right)\exp\left(\frac{-\Delta H_a}{R \times T}\right) \quad (11)$$

Activation energy denoted as E_a along with the Arrhenius pre-exponential factor, represented by A, and constants like the universal gas constant (R) and absolute temperature (T), are fundamental parameters in understanding reaction kinetics. In addition, Avogadro's number (N) and the Planck constant (h) play crucial roles in theoretical frameworks. Activation entropy

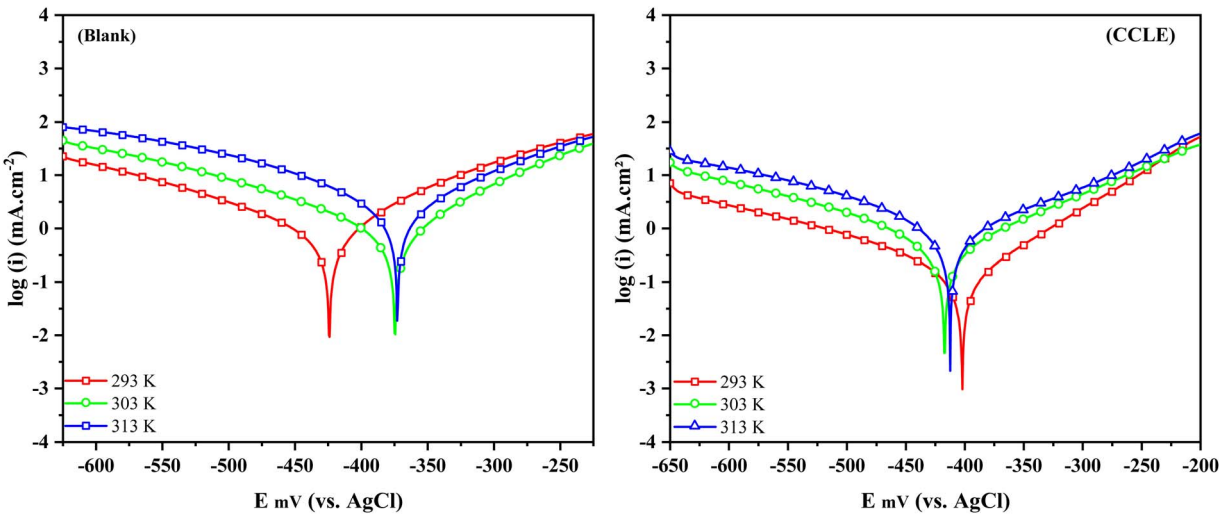

Fig. 6 Potentiodynamic polarization (PDP) curves recorded under various temperature conditions, both in the presence and absence of CCLE, within a 1 M HCl solution.

Table 5 Tafel parameters of the carbon steel at various temperatures with the incorporation of the CCLE inhibitor

Medium	Temperature (K)	E_{corr} *vs.* AgCl (mV)	i_{corr} (mA cm^2)	β_a (mV dec^{-1})	$-\beta_c$ (mV dec^{-1})	I.E$_{PDP}$%
Blank	293	−421.37 ± 0.57	0.73 ± 0.05	81.10 ± 1.61	119.33 ± 1.20	—
	303	−373.6 ± 1.64	1.09 ± 0.06	88.77 ± 2.79	122.33 ± 1.5	—
	313	−370.53 ± 1.5	2.17 ± 0.09	99.8 ± 2.55	113.13 ± 2.52	—
CCLE	293	−397.2 ± 3.2	0.16 ± 0.01	83.60 ± 1.60	139.40 ± 8.80	78
	303	−412.6 ± 8.9	0.22 ± 0.04	80.20 ± 5.09	124.63 ± 3.20	79.2
	313	−412.9 ± 6.7	0.33 ± 0.03	109.47 ± 7.49	118.33 ± 6.12	84.5

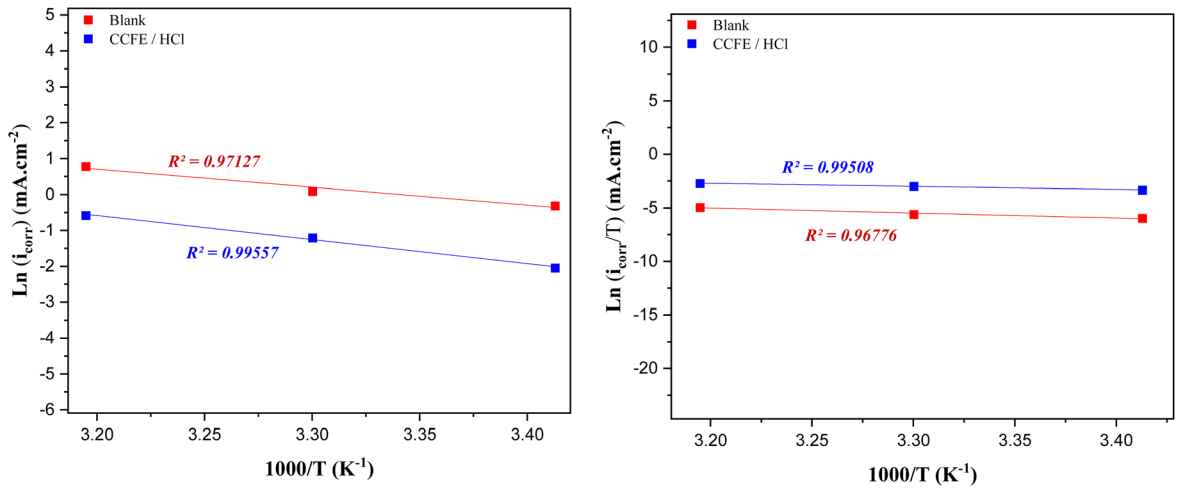

Fig. 7 Arrhenius plots and ln(i_{corr}/T) *versus* 1000/T graphs created for carbon steel (CS) immersed in 1 M HCl, both with and without the addition of CCLE.

(ΔS_a) and enthalpy (ΔH_a) further illuminate the energetics of reactions. Arrhenius plots, as illustrated in Fig. 7, provide graphical insights into both inhibited and uninhibited media. These plots offer a theoretical lens to understand the adsorption coordination process between CCLE constituents and specimen active sites. Results tabulated in Table 6 reveal that activation energy values, derived from ln(i_{corr}) *vs.* 1000/T plots, increase upon CCLE introduction, suggesting adsorption occurs at active centers with lower energies, while metal dissolution takes place at those with higher energies. This underscores a chemical coordination between inhibitor molecules and the carbon steel surface.[75] Moreover, activation enthalpy and entropy parameters, computed from ln(i_{corr}/T) *vs.* 1000/T plots (Table 6), shed light on the endothermic nature of steel dissolution, indicated by positive ΔH_a values, whether in the presence or absence of CCLE, contributing to its sluggish rate.[76] Notably, the rise in activation entropy in the presence of CCLE molecules signifies a more orderly prohibitive layer has been developed associated with the formation of the steel-CCLE complex.[77]

Table 6 Entropy, enthalpy, and activation energies with and without the incorporation of CCLE

	E_a (kJ mol^{-1})	ΔH_a (kJ mol^{-1})	ΔS_a (J mol^{-1} K^{-1})
Blank	41.86	39.17	−114.1
CCLE	33.35	30.68	−188.5

3.5 Synergetic effect

Synergistic studies were conducted to enhance the inhibitory efficiency of *Chrysanthemum coronarium* leaf extract (CCLE) on carbon steel in 1 M HCl medium using potassium iodide (KI/6 10^{-3} M) at both minimal and maximal concentrations of the extract. Potentiodynamic polarization and electrochemical impedance spectroscopy were employed at 293 K to assess the effectiveness of this combination. Graphical parameters and polarization resistance data obtained from Tafel extrapolation during potentiodynamic polarization evaluations, both in the presence and absence of the leaf extract in the solution, are presented in Fig. 8 and Table 7. The curves reveal no significant alteration in the shape of the cathodic and anodic branches in the presence of CCLE with KI. However, a notable decrease in the β_a and β_c slope values is observed in the presence of CCLE with KI, indicating that the introduction of both compounds mitigates the corrosion process, both in the anodic region for metal dissolution and in the cathodic region for hydrogen evolution. Additionally, i_{corr} values also decrease for both concentrations when the extract and halide are present, indicating strengthened inhibitory effects, reaching 87.7% in an acidic medium with 2 g L^{-1} of CCLE, demonstrating significant synergistic interaction between the halide ions and

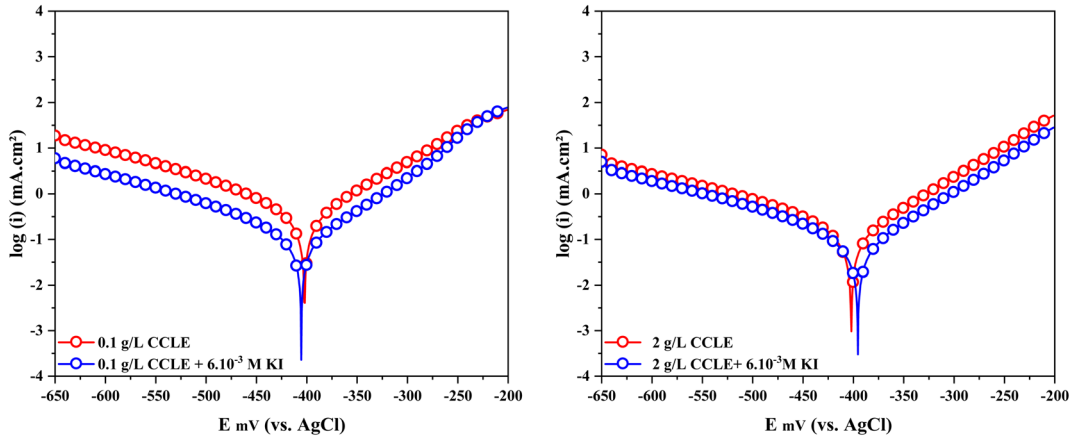

Fig. 8 Tafel curves depicting the performance of carbon steel in the presence and absence of both potassium iodide (KI) and CCLE.

Table 7 The corrosion rate features of the carbon steel influenced by the presence and absence of the CCLE inhibitor and potassium iodide (KI)

Concentration	E_{corr} *vs.* AgCl (mV)	i_{corr} (mA cm^2)	β_a (mV dec^{-1})	$-\beta_c$ (mV dec^{-1})	I.E$_{PDP}$ (%)
Blank	−421.37 ± 0.57	0.73 ± 0.05	81.10 ± 1.6	119.33 ± 1.2	—
Blank + 6 × 10^{-3} M KI	−360.23 ± 2.01	0.44 ± 0.02	70.77 ± 2.4	124.93 ± 4.2	40
0.1 g per L CCLE	−401.8 ± 3.8	0.38 ± 0.01	101.00 ± 8.35	133.10 ± 3.89	47.9
0.1 g per L CCLE + 6 × 10^{-3} M KI	−392.3 ± 4.2	0.16 ± 0.01	80.47 ± 4.35	89.53 ± 6.43	78
2 g per L CCLE	−397.2 ± 3.2	0.16 ± 0.01	83.60 ± 1.60	139.40 ± 8.80	78
2 g per L CCLE + 6.10^{-3}M KI	−391.8 ± 6.8	0.09 ± 0.01	73.53 ± 4.32	−94.53 ± 4.51	87.7

Chrysanthemum coronarium leaf extract compounds. Fig. 9 and Table 8 illustrate the collected EIS analysis data. In the presence of CCLE with KI, the capacitive loop's semicircle significantly increases compared to CCLE alone in the acidic medium, with no significant modification in shape. The polarization resistances recorded in Table 8 attest to this improvement. When the leaves extract concentration associated with halide ions is lowest, R_p increases from 45.01 to 98.87 Ω cm^2 due to increased compound adsorption on the steel surface, resulting in a significant decrease in capacitance. Similar results were obtained for the maximum concentration of CCLE associated with the halide ion, where inhibitory efficiency appears significantly increased in the presence of both compounds. These electrochemical results are confirmed by these observations, indicating that the combination of KI and CCLE significantly reduces the corrosive effect of the acidic environment. The synergy observed between the simultaneous presence of corrosion inhibitors and iodide ions can be explained either by a competitive adsorption mechanism between these substances, where each opposes the other for adsorption sites on the surface, leading to their simultaneous coating, or by a cooperative mechanism where one compound chemisorbs to

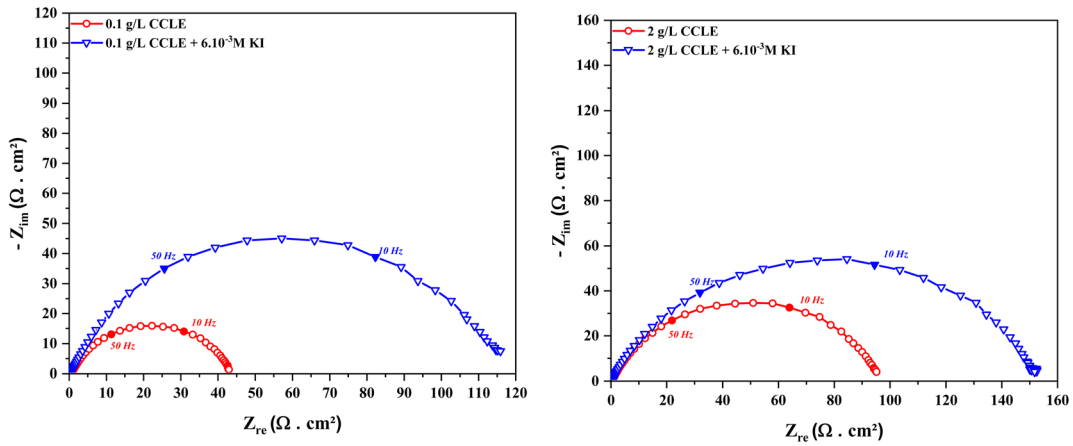

Fig. 9 Nyquist plots illustrating the behavior of carbon steel when subjected to 1 M HCl with the addition of both potassium iodide (KI) and CCLE.

Table 8 EIS assessments conducted for the working electrode immersed in a 1 M HCl at 293 K, with both potassium iodide (KI) and CCLE simultaneously present

			CPE				
Concentration	R_s (Ω cm^2)	R_p (Ω cm^2)	Q ($\mu\Omega^{-1}$ s^n cm^{-2})	n	C (μF cm^{-2})	χ^2	I.E$_{EIS}$ (%)
Blank	0.81 ± 0.01	25.47 ± 0.12	424 ± 0.36	0.83 ± 0.01	168	0.002	—
Blank + 6 × 10^{-3} M KI	0.76 ± 0.01	44.3 ± 2.35	344 ± 0.15	0.81 ± 0.01	129	0.004	42.5
0.1 g per L CCLE	0.92 ± 0.17	45.01 ± 2.54	335 ± 0.1	0.79 ± 0.01	109.8	0.001	46
0.1 g per L CCLE + 6.10^{-3}M KI	0.83 ± 0.07	116.0 ± 1.34	150 ± 0.01	0.82 ± 0.01	61.6	0.001	78
2 g per L CCLE	0.73 ± 0.01	98.87 ± 6.62	18 ± 0.05	*0.78* ± 0.01	57.7	0.001	74.2
2 g per L CCLE + 6 × 10^{-3} M KI	0.81 ± 0.08	149.8 ± 3.95	141 ± 0.02	0.79 ± 0.01	50.5	0.001	83

Table 9 Synergistic parameter of CCLE and KI in a 1 M hydrochloric acid solution through EIS and PDP analysis

	PDP		EIS	
Concentration	I.E$_{PDP}$ (%)	S_{PDP}	I.E$_{EIS}$ (%)	S_{EIS}
6 × 10^{-3} M KI	40	1.12	42.5	1.13
0.1 g per L CCLE	47.9		46	
0.1 g per L CCLE + 6 × 10^{-3} M KI	78		78	
6 × 10^{-3} M KI	40		42.5	
2 g per L CCLE	78	1.35	74.2	1.4
2 g per L CCLE + 6 × 10^{-3} M KI	87.7		83	

an active center while the second undergoes physisorption,[78] facilitating their combined action, as follows:

$$S = \frac{1 - \left(\eta + \eta^{'}\right)}{1 - \eta^{''}} \quad (12)$$

where S, η, η', η'' are the synergistic parameter, the inhibitory efficiency in the presence of KI, CCLE, and CCLE combined with the halide catalyst, respectively. According to Table 9, the calculated synergistic parameter exceeds unity for both extract concentrations, highlighting that the incorporation of *Chrysanthemum coronarium* leaf extract and halide ions markedly diminishes the corrosion rate of carbon steel in a hydrochloric medium. This reduction is attributed to the formation of a predominant protective layer at the interface, facilitated by the synergistic interaction between the two compounds.

3.6 Adsorption isotherm

Exploring adsorption isotherms remains a valuable method for deepening our understanding of the chemical interactions between corrosion inhibitors and metal surfaces. Typically, organic molecules hinder corrosion by attaching to the metal's active surface, displacing water molecules initially present on that surface. This process forms a protective layer that restricts corrosive agents' access to the metal surface. To investigate the interaction between a corrosion inhibitor (CCLE) and the metal surface in an HCl environment, various isotherms such as Langmuir, Frumkin, and Temkin were exploited to analyze the adsorption dynamics at the interface as follows:[79,80]

$$\text{Langmuir}: \ \frac{C_{inh}}{\theta} = \frac{1}{K} + C_{inh} \quad (13)$$

$$\text{Temkin}: \exp(-2a\theta) = KC_{inh} \quad (14)$$

$$\text{Frumkin}: \ \left(\frac{\theta}{1-\theta}\right)\exp(-2a\theta) = KC_{inh} \quad (15)$$

$$\theta = \frac{i^0_{corr} - i^{inh}_{corr}}{i^0_{corr}} \quad (16)$$

Within this framework, the symbol K denotes the equilibrium adsorption constant, which reflects the affinity of the corrosion inhibitor for the metal surface. The parameter θ signifies the fractional surface coverage, indicating the proportion of the metal surface occupied by the inhibitor molecules. Additionally, the symbol a represents the constant of molecular interaction, portraying the strength of the interactions between the inhibitor molecules and the metal surface. Analysis of the adsorption isotherms suggests that the introduction of CCLE prompts the expulsion of water atoms from the metal surface's active locations. Consequently, a suppressive monolayer form on the metallic surface aligns with the Langmuir isotherm model. This model assumes that a fixed number of active sites exist on the adsorbent's surface, each capable of accommodating only one adsorbate molecule.[81] As a result, adsorption occurs in a manner that forms a monolayer of inhibitor molecules without lateral interactions between them. However, the Langmuir model's simplicity encounters challenges when applied to complex systems like plant extracts, which contain a multitude of compounds with diverse chemical structures. The intricate composition of CCLE makes it arduous to designate a specific inhibitory action for the extract. This complexity hinders the straightforward determination of the thermodynamic properties of the extract's compounds. Nevertheless, employing an isotherm model facilitates the exploration of the thermodynamic properties by evaluating the equilibrium constant K_{ads}. This constant characterizes the equilibrium between the adsorbed and unadsorbed inhibitor molecules on the metal surface. Despite its utility, the phytochemical diversity of the CCLE presents a significant challenge in accurately determining its molecular weight. Consequently, this complexity complicates the precise determination of the solution's molarity, affecting the interpretation of experimental results and the formulation of effective corrosion inhibition strategies (Fig. 10).[17,73,82,83]

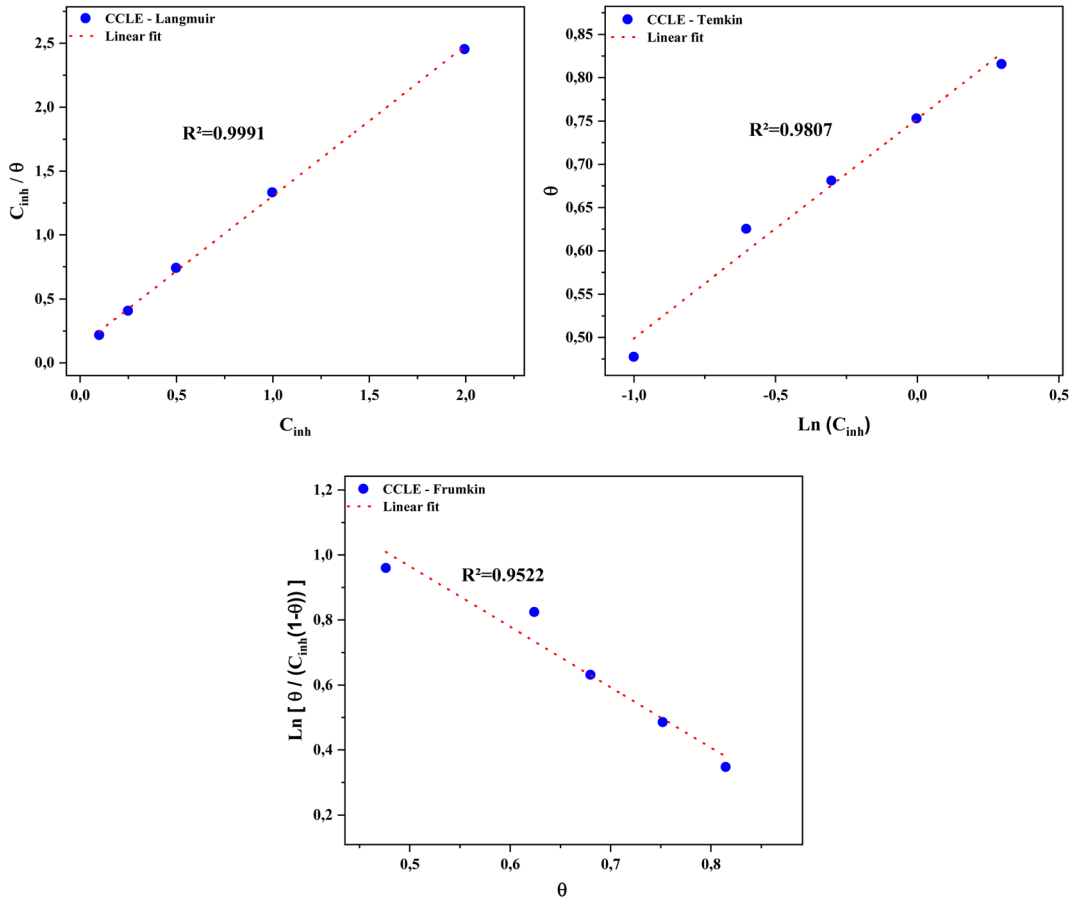

Fig. 10 Isotherm model graphs depicting the interaction of CCLE with carbon steel in a 1 M HCl solution at 293 K.

3.7 SEM-EDX study

For further exploration of the influence of phytoconstituents derived from the *Chrysanthemum coronarium* leaves extract on the surface of carbon steel in an acidic environment, a 15 hours thorough surface investigation was carried out using the SEM-EDX method at 293 K. The state of the steel surface under various testing settings is clearly shown by the SEM pictures, as shown in Fig. 11. When as opposed to the unexposed metal surface, it is clear that the steel surface shows considerable damage in the absence of CCLE, which is shown by the presence of pits and fractures. This damage is a result of the continuous metallic breakdown process in the acidic medium. Nevertheless, a notable inhibition of the corrosion process is seen after adding CCLE to the mixture. There is a discernible decrease in the frequency of local corrosion pits, and the surface seems to be insulated. The EDX data, which is compiled in Table 10, supports this conclusion even more. The examination of the data indicates that there are significant oxygen atoms on the steel surface in the inhibited medium. These atoms are often linked to the production of ferrous oxide as a consequence of the corrosion process. It's interesting to note that the fraction of oxygen atoms connected to the corrosion by-product decreases when CCLE is added to the medium (Fig. 12). This implies that the leaf substances found in *Chrysanthemum coronarium* plants have the capacity to mitigate the pace at which carbon steel dissolves in a hydrochloric solution. This outcome is likely a result of the cohesive interaction between these compounds and the active centers residing on the C38 active surface. This interaction facilitates the formation of a protective layer, effectively hindering the corrosive action of the environment on the metal surface.

3.8 Analysis of DFT results

Continuing our investigation into the constituents of *Chrysanthemum coronarium* stems and flower extracts[17,82] this study focuses on the DFT analysis of the components found in the leaf extract. Illustrated in Fig. 1, these components include: **L1** – chlorogenic acid, **L2** – 4,5-dicaffeoylquinic acid, **L3** – 3,4-dicaffeoylquinic acid, **L4** – 3,5-dicaffeoylquinic acid, **L5** – 4-succinyl-3,5-dicaffeoylquinic acid, and **L6** – rutin. Notably, **L1** and **L6** are also present in the stem and flower extracts, thus their results are included solely for comparative purposes with the other components of the leaf extract. Comprehensive discussions regarding their HOMOs, LUMOs, and ESP maps were previously provided.[17,82] Moreover, due to their isomeric nature, the electronic properties of **L2**, **L3**, and **L4** are nearly identical.

3.8.1 Analysis of HOMOs, LUMOs, ESP maps. Fig. 13 illustrates the optimized structures, HOMOs, LUMOs, and

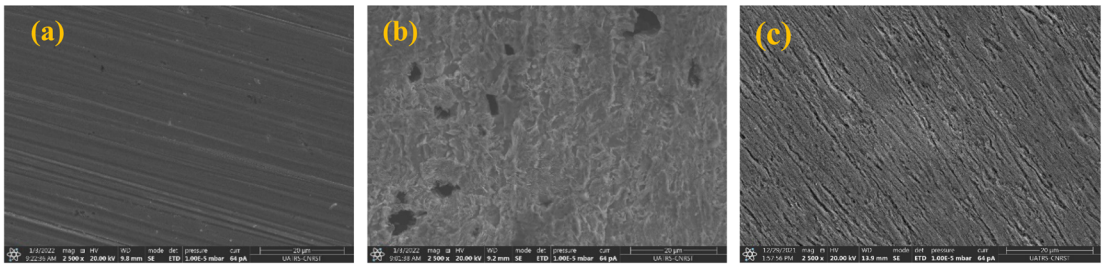

Fig. 11 SEM images depicting carbon steel are presented as follows: (a) in its original, untreated state, (b) after immersion in 1 M HCl, and (c) after exposure to 1 M HCl containing 2 g L^{-1} of CCLE.

Table 10 Atom percentage recorded in the EDX spectrum with the incorporation of CCLE

	Atom percentage			
Conditions	Iron	Carbon	Oxygen	Total
1 M HCl	86.95	6.9	6.14	100
1 M HCl + CCLE	91.32	6.57	2.11	100

electrostatic potential maps (ESP) of the *Chrysanthemum coronarium* stem and flower extracts (**L1–L6**). Notably, for **L2**, **L3**, and **L4**, the HOMO is predominantly localized over one of the dicaffeoylic acid units, whereas their LUMOs are spread across both units of the dicaffeoylic acid. Similarly, for the L5 inhibitor, the findings indicate that the HOMO is also concentrated over one of the dicaffeoylic acid units, while the LUMO is dispersed over the other dicaffeoylic acid unit. These results shed light on the electron donation tendency of one dicaffeoylic acid unit to the metal surface, while the other exhibits a susceptibility to accept electrons from the metal surface.

Plotting of the ESP maps can give additional insight into the electron-rich and electron-poor regions. The strong red color (negative potential) covers the carbonyl oxygen atom region of the dicaffeoylic acid units, while the strong blue color (positive potential) covers the carbonyl carbon atom. In addition, the faint red color (weak negative potential) covers the aromatic ring of the dicaffeoylic acid unit. The red regions represent the nucleophilic regions, which are electron-rich and are subjected to electrophilic attacks. On the contrary, the blue region corresponds to the electrophilic region, which are electron-poor centers and they are the favorable sites for nucleophilic attacks. Again, these results are also confirmed by plotting the total densities at the HOMOs and LUMOs as shown in Fig. SD1 of the ESI.† The red and blue trajectories correspond to the electron-rich and electron-poor regions, which are responsible for electrophilic and nucleophilic attacks, respectively.

3.8.2 Analysis of global chemical reactivity descriptors. The energies of HOMO and LUMO of the inhibitor molecules (E^{inh}_{HOMO} and E^{inh}_{LUMO}) are quantum chemical descriptors, which are usually related to the electron donating and accepting

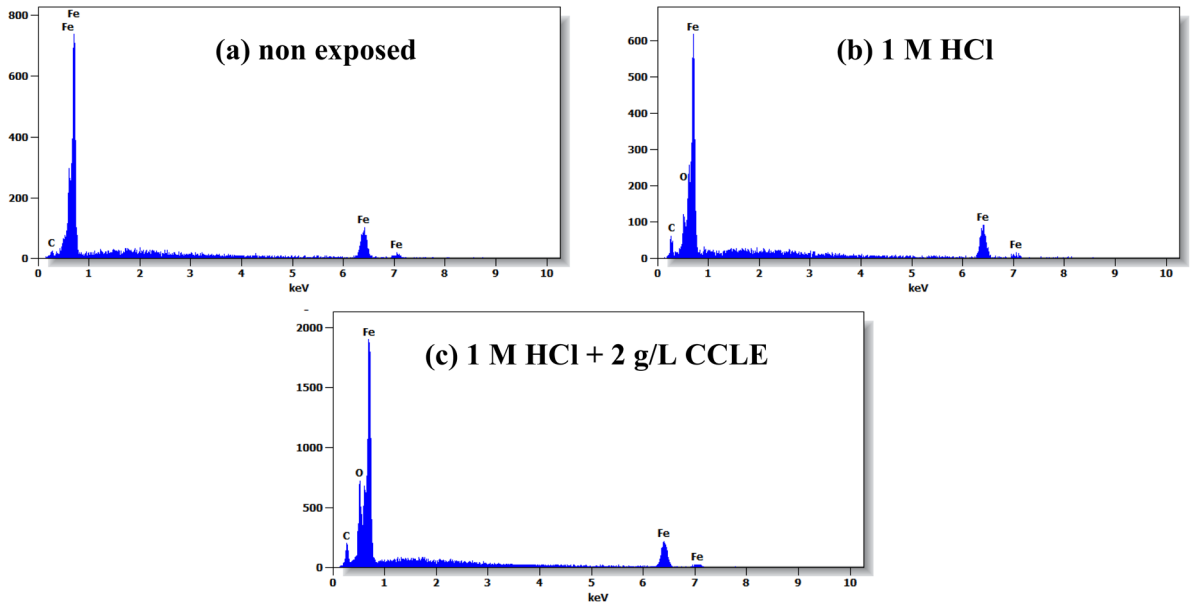

Fig. 12 EDX analysis results for carbon steel are provided for (a) its original state, (b) after immersion in 1 M HCl, and (c) after exposure to 1 M HCl with the addition of 2 g L^{-1} of CCLE.

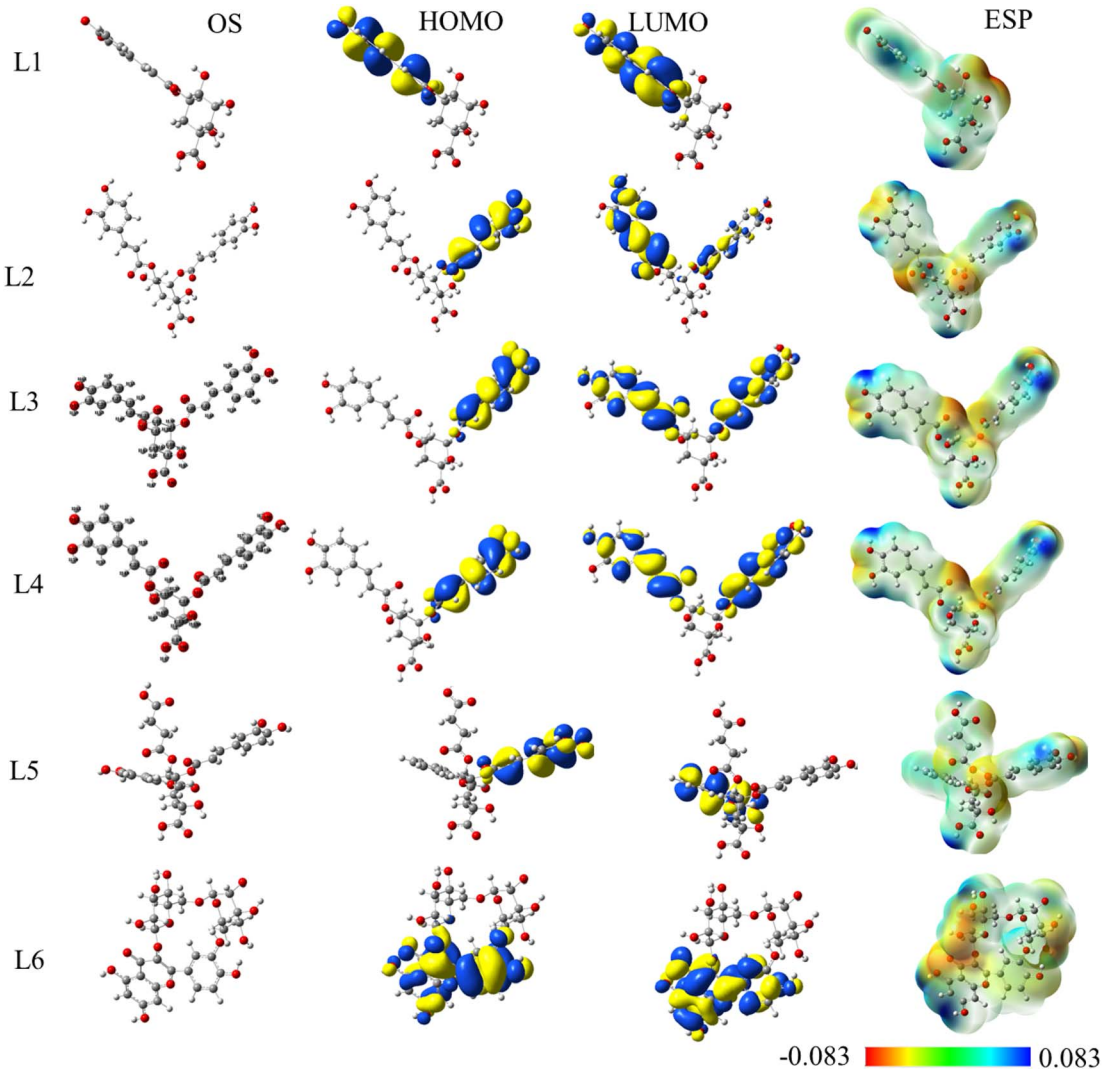

Fig. 13 From left to right: optimized molecular structures, HOMOs, LUMOs, and electrostatic potential (ESP) maps for the components of the *Chrysanthemum coronarium* leaves extract as obtained using the B3LYP/6-31+G(d,p) level of theory in aqueous solution.

tendency of the inhibitor molecules. Thus, inhibitors having high values of E^{inh}_{HOMO} incline to donate electrons to the unoccupied 3d-orbitals of the metal acceptors, while the lower E^{inh}_{LUMO} value, the higher ability to accept electrons from the occupied 3d-orbital of the metal. On the other hand, when the metaland inhibitor become close to each other, this permits the electrons to flow from the inhibitor to the metal or *vice versa*. Table 11 displays the values of E^{inh}_{HOMO}, E^{inh}_{LUMO}, ΔE_1 and ΔE_2. To simplify the representation of the results, the graphical representation of the ΔE, ΔE_1, and ΔE_2 are shown in Fig. 14.

According to the E^{inh}_{HOMO} values in Table 12 and Fig. 14, the following order of electron-donating ability from the inhibitor to the metal surface is accepted as follows: **L6** > **L2** > **L4** > **L3** > **L5** > **L1**. Whereas, according to E^{inh}_{LUMO}, order of accepting electron ability power from the metal is given as follows: **L5** > **L1** > **L3** > **L4** > **L2** > **L6**.

The energy gap is an important quantum global descriptor, which measures the chemical reactivity and kinetic stability of the molecule. The lower the energy gap, the higher the chemical reactivity and the lower the chemical kinetic stability. Results in Table 11 and shown in Fig. 14 declare the following chemical reactivity order as follows: **L5** > **L3** > **L4** > **L2** > **L1** > **L6**. Therefore, among the investigated inhibitors, **L5** has the highest corrosion inhibition efficiency, while L6 has the lowest corrosion inhibition efficiency.

Table 11 Energy gaps (ΔE), metal → inhibitor (ΔE_1) and inhibitor → metal (ΔE_2) interactions of for the components of the *Chrysanthemum coronarium* leaves extract as obtained using the B3LYP/6-311+G(d,p) level of theory in aqueous solution

	E^{inh}_{HOMO}	E^{inh}_{LUMO}	ΔE	ΔE_1	ΔE_2
L1	−6.129	−2.177	3.951	5.835	5.925
L2	−6.096	−2.157	3.940	5.725	5.978
L3	−6.102	−2.173	3.929	5.701	5.951
L4	−6.099	−2.164	3.936	5.746	5.945
L5	−6.102	−2.327	3.775	5.746	5.945
L6	−6.076	−2.068	4.009	5.739	5.948

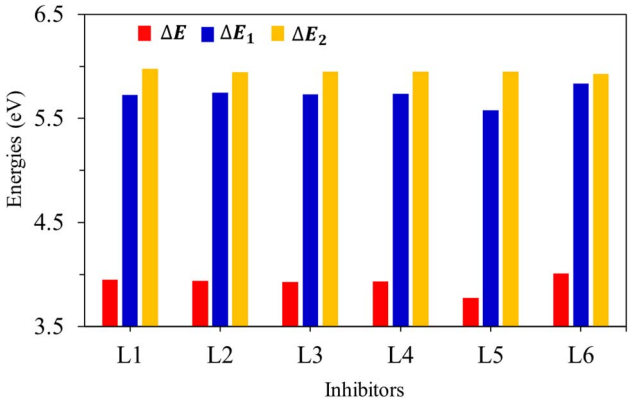

Fig. 14 Energy gaps, ΔE, metal → inhibitor (ΔE_1) and inhibitor → metal (ΔE_2) interactions for the components of the *Chrysanthemum coronarium* leaves extract as obtained using the B3LYP/6-311+G(d,p) level of theory in aqueous solution.

The electron flow ability from metal to inhibitor or *vice versa* can be explained by calculating ΔE_1 and ΔE_2 descriptors. The results are also tabulated in Table 11 and graphically shown in Fig. 14. Our results reveal that for all investigated inhibitors, the $\Delta E_1 < \Delta E_2$, signifying that the metal acts as Lewis base and the inhibitors act as Lewis acids. Therefore, the ability to electron from form the occupied 3d-orbitals of the metal to the lying unoccupied orbitals of the inhibitors is energetically favored compared to the reverse process. Among all the investigated inhibitors, the ability to electron flow from metal to inhibitor (ΔE_1) is ordered as follows: **L5** > **L1** > **L3** > **L4** > **L2** > **L6**, while the tendency to electron flow from inhibitor to metal (ΔE_2) is ordered as follows: **L6** > **L2** > **L4** > **L3** > **L5** > **L1**.

The vertical ionization potential and the vertical electron affinity have been used to calculate the most relevant global chemical reactivity descriptors for all components of the *Chrysanthemum coronarium leaves* extract as obtained using the B3LYP/6-311+G(d,p) level of theory in aqueous solution and results are summarized in Table 12.

It was reported that the inhibitors with low electronegativity value have a good corrosion inhibition performance. Based on this assumption and monitoring our results in Table 11, the expected corrosion inhibition efficiency is as follows: **L5** > **L6** > **L2** > **L3** ≈ **L4** > **L1**. Considering the change in electronegativity of Fe metal ($\chi_{Fe} = 7.0$ eV) and the inhibitor as $\Delta\chi\chi_{Fe} - \chi_{inh}$, the following order is expected for increasing of $\Delta\chi$ as follows: **L5** (2.918 eV) > **L6** (2.915 eV) > **L2** (2.850 eV) > **L3** (2.841 eV) ≈ **L4** (2.841 eV) > **L1** (2.820 eV). Consistent with Sanderson's electronegativity equalization principle,[84] **L5** and **L6** with the lowest χ and highest $\Delta\chi$ values and hence high reactivity are expected to have the highest corrosion inhibition efficacy.

It was reported by Obi-Egbedi *et al.*[85] that a hard molecule has a larger energy gap, while a soft molecule has a small energy gap. According to our results of hardness and softness, as shown in Table 12, the corrosion inhibition efficiency of the investigated inhibitor is ordered as follows: **L5** > **L3** > **L2** > **L4** > **L1** > **L6**. Therefore, **L5** and **L3** inhibitors are the most active components for the protection of the metal surface against corrosion.

The tendency of chemical species to accept electrons can be measured by calculating the electrophilicity index (ω). It was reported that as the ω increases, the tendency behavior of the molecule to accept electrons increases. Thus, a good electrophile is characterized by higher values of μ and ω, while, on the contrary, a good nucleophile is known for its low values of μ and ω. Asindicated in Table 12, the corrosion inhibition efficiency ranking of the different components is given as follows: **L5** > **L3** > **L1** > **L4** > **L2** > **L6**.

The set of eqn (4) has been used to calculate the values of the electron-accepting tendency (ω^-), electron-donating behavior (ω^+), and net electrophilicity ($\Delta\omega^{\pm}$) for all components of the *Chrysanthemum coronarium leaves* extract as obtained using the B3LYP/6-311+G(d,p) level of theory in aqueous solution, and the results are also summarized in Table 12. The results obtained revealed that the order of electron-donating power follows the order **L5** > **L3** > **L1** > **L4** > **L2** > **L6**, and the same order is also achieved for the electron-accepting power and the net

Table 12 Quantum chemical reactivity descriptors for all components of the *Chrysanthemum coronarium* leaves extract as obtained using the B3LYP/6-311+G(d,p) level of theory in aqueous solution. Softness and nucleophilicity are in the eV^{-1} unit, dipole moment in Debye, ΔN_{110} is unitless, and the other descriptors are in the eV unit

	L1	L2	L3	L4	L5	L6
E_0	−35311.751	−50884.298	−50884.293	−50884.298	−61239.972	−61243.003
E_0^-	−35314.071	−50886.607	−50886.635	−50886.610	−61242.693	−61245.210
E_0^+	−35305.711	−50878.308	−50878.306	−50878.292	−61234.530	−61237.041
I_v	6.040	5.990	5.987	6.006	5.442	5.961
A_v	2.321	2.309	2.342	2.312	2.721	2.208
μ	−4.180	−4.150	−4.165	−4.159	−4.082	−4.085
χ	4.180	4.150	4.165	4.159	4.082	4.085
η	1.860	1.840	1.822	1.847	1.361	1.877
σ	0.538	0.543	0.549	0.542	0.735	0.533
ω	4.698	4.678	4.759	4.684	6.123	4.444
ε	0.213	0.214	0.210	0.214	0.163	0.225
ω^-	7.021	6.983	7.069	6.994	8.333	6.721
ω^+	2.841	2.833	2.905	2.835	4.252	2.637
$\Delta\omega^{\pm}$	9.861	9.817	9.974	9.829	12.585	9.358
$\Delta E_{b\text{-}d}$	0.172	0.182	0.180	0.179	0.271	0.196
ΔN_{110}	−0.465	−0.460	−0.456	−0.462	−0.340	−0.469

electrophilicity. Therefore, these results indicate that **L5** and **L3** inhibitors have the highest possibility to accept and donate electrons simultaneously. Whereas, **L6** is characterized by the lowest ω^-, ω^+, and $\Delta\omega^{\pm}$.

Another quantum chemical descriptor is the $\Delta E_{b\text{-}d}$, which describes the transfer of charge from a molecule, followed by its return to the molecule. González Gómez *et al.*[86] proposed that the $\Delta E_{b\text{-}d}$ value is decreased and becomes energetically favored with the increase in the harness value. In addition, as $\Delta E_{b\text{-}d}$ becomes less negative, the corrosion inhibition efficiency of the molecule increases. As indicated from the results in Table 11, the corrosion inhibition efficacy of the investigated components can be arranged as follows: **L5** > **L3** > **L2** > **L4** > **L1** > **L6**.

As the metal and inhibitor become close to each other, electrons can flow from an inhibitor with lower χ to a metal with higher χ, until equilibrium is reached ($\chi_{in} = \chi_{Fe}$). Therefore, at this point, the fraction of electrons transferred, ΔN_{max}, is given by eqn (17).

$$\text{The fraction of transferred electron}(\Delta N_{110}) \quad \Delta N_{110} = \frac{(\chi_{Fe} - \chi_{inhibitor})}{2(\eta_{Fe} + \eta_{inhibitor})} \tag{17}$$

Here, $\chi_{Fe} = 7.0$ eV,[87] and the global hardness ($\eta_{Fe} = 0$) for iron, considering $I = A$ for metallic bulk atoms.[88] Recent studies reported that using $\chi_{Fe} = 7.0$ eV is not correct, and instead, the work function of Fe metal ($\Phi_{Fe} = 4.82$ eV for Fe_{110} plane) is used.[89]

$$\text{The fraction of transferred electron}(\Delta N_{110}) \quad \Delta N_{110} = \frac{(\Phi_{Fe} - \chi_{inhibitor})}{2(\eta_{Fe} + \eta_{inhibitor})} \tag{18}$$

Eqn (10) provides a more accurate measure of ΔN_{110} then using $\chi_{Fe} = 7$ eV because it is considered without accounting for electron–electron interactions but for the free electron gas Fermi energy of iron only.[89,90] The results obtained for ΔN_{110} are also summarized in Table 12. It was outlined previously that the positive value (ΔN_{110}) indicates that the inhibitors act as electron donors (Lewis base)[91,92] Inspection of Table 12 indicates that ΔN_{110} values for species are positive and <3.6 values,[92] illustrating that all of the inhibitors have the ability to donate electrons to the unoccupied 3d-orbital of the Fe metal. Additionally, our results show that **L5** and **L6** molecules have the greatest ΔN_{110} values of 0.271 and 0.196, respectively followed by **L2**, **L3**, and **L4** with ΔN_{110} values of 0.182, 0.180 and 0.179, respectively, while **L5** has the smallest ΔN_{110} value of 0.172. As can be seen, **L2–L4** inhibitors have almost the same ΔN_{110} values, which can be attributed to their similar structures as isomers.

3.8.3 Analysis of local reactivity indices. FFs, which were originally introduced by Kenichi Fukui, are a concept[53] that considers the effects of structural differences on the reactivity of the different active centers in the molecule. Fukui's theory explains the behavior of electrons in a molecule when exposed to small perturbations.[53,84] Fukui functions are valuable tools for pinpointing specific regions or atoms within a molecule that exhibit nucleophilic or electrophilic characteristics, indicating their roles in donating or accepting electrons.[38,51,84] Fig. 15 shows the 3D iso-surfaces of the Fukui functions for the most active electrophilic ($f^-(r)$), electrophilic ($f^+(r)$) and dual ($f^2(r)$ attacks centers of the investigated inhibitor molecule.

To measure the Fukui functions, Hirshfeld charges were employed to derive the condensed Fukui descriptors for both nucleophilic (f_k^+) and electrophilic (f_k^-) interactions, along with the dual condensed Fukui descriptor (f_k^2) based on conceptual density functional theory (CDFT)[93,94] as implemented in the Multiwfn code[95] using the following equations:[84]

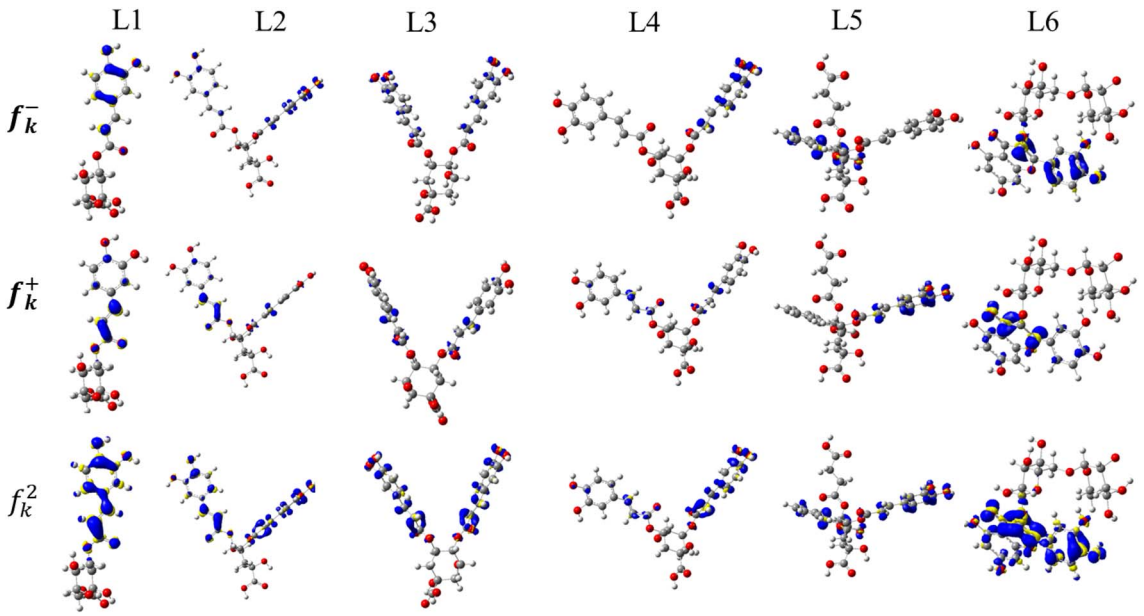

Fig. 15 3D-isosurfaces (isovalue = 0.005 a.u.) of the electrophilic, nucleophilic, and dual attacks for the components of the *Chrysanthemum coronarium* leaves extract as obtained using the B3LYP/6-311+G(d,p) level of theory in aqueous solution.

$$f_k^+ = q_k^N - q_k^{N+1}, f_A^- = q_k^{N-1} - q_k^N, \text{ and } f_k^2 = f_k^+ - f_k^- \quad (19)$$

Here, q_N^A, q_{N+1}^A and q_{N-1}^A are the Hirshfeld charges over the k atom for systems with N, $N+1$, and $N-1$ electrons, respectively. The strong electrophile character at an atom k is measured by the maximum value of the f_k^+ descriptor indicates a strong electrophilic character, while the strong nucleophilic character at atom k is identified by the maximum value of f_k^- descriptor.[96] Morell *et al.*[97] introduced the most accurate descriptor, known as the condensed dual Fukui descriptor (f_k^2), which extends the understanding of the f_k^+ and f_k^- indices and objects to describe concurrently the nucleophilic and electrophilic potencies at an atomic site. Morell *et al.*[97] reported that if $f_A^2 > 0$, an atom's tendency to undergo nucleophilic attack designates it as a favored location for donating electrons.

Contrary, $f_A^2 < 0$ indicates the atom's ability to undergo electrophilic attack, making it a preferred site for accepting electrons.[97,98] Fig. 16 graphically presents the most representative results of the condensed Fukui indices for nucleophilic (f_A^+), electrophilic (f_A^-), and (f_A^2) dual interactions of the investigated leaves compounds. The most representative results of the condensed Fukui nucleophilic (f_A^+), electrophilic (f_A^-) and dual (f_A^2) indices of the investigated phytochemical compounds are graphically shown in Fig. 16. In order to follow up on the number of active centers, Fig. SD2† shows the optimized structures of the probed inhibitors with the number of atoms. The complete results, including the Hirshfeld charges for the N, $N+1$, and $N-1$ electron systems, as well as the condensed Fukui indices for nucleophilic (f_A^+), electrophilic (f_A^-), and dual interactions ($f_A^{2)}$ of the examined inhibitor molecules, are summarized in Tables SD1–SD6 of the ESI.† In this study, we are dealing only with the results of f_A^2. For **L1** inhibitor, the most active centers for electrophilic attacks are correspondingly, O9, C20, and O8, while the centers that are active for nucleophilic attacks are C19 and C17, respectively, see Fig. 16a and Table SD1†. For **L2** inhibitor, as indicated in Fig. 16b and Table SD2,† the centers O11, O9, and C26 show the maximum propensity for electrophilic attacks, respectively, while the most favorable centers for nucleophilic

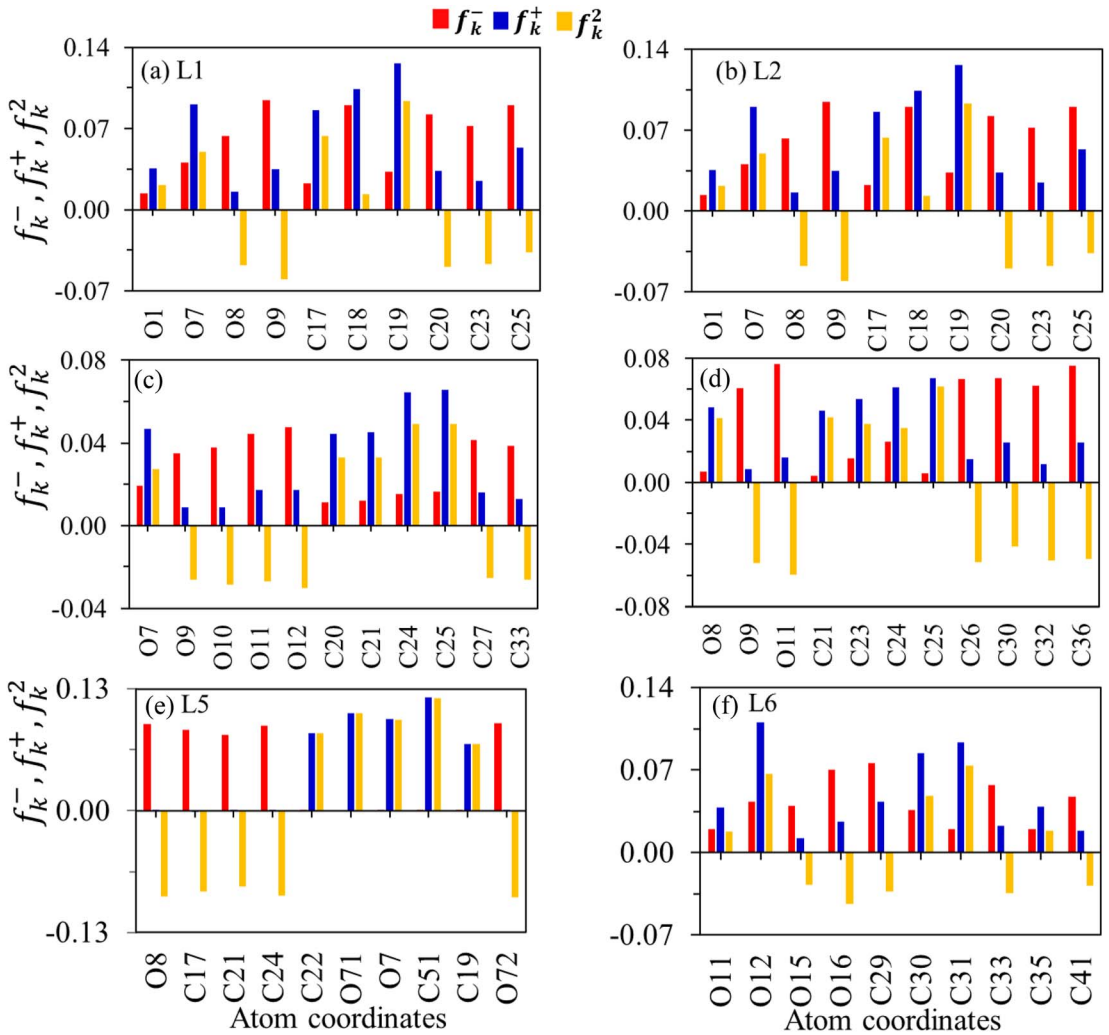

Fig. 16 Condensed Fukui functions for nucleophilic, electrophilic, and dual attacks (a)–(f) for the components of the *Chrysanthemum coronarium* leaves extract as obtained using the B3LYP/6-311+G(d,p) level of theory in aqueous solution.

attacks are, correspondingly, C25 and C21. For the **L3** inhibitor, the results shown in Fig. 16c and listed in Table SD3† declare that the centers O12 and O10 have the highest tendency to undergo electrophilic attacks, while the C24 and C25, C20 and C21 atoms show the maximum capability to undergo nucleophilic attacks. For the **L4** inhibitor, our results show that the centers O11 and O9 undergo electrophilic attacks, while the C25 and C24 can undergo nucleophilic attacks, see Fig. 16d and Table SD4.† The results listed in Table SD5† and shown in Fig. 16e for the **L5** inhibitor indicate that O72 and O9 have the maximum ability to undergo

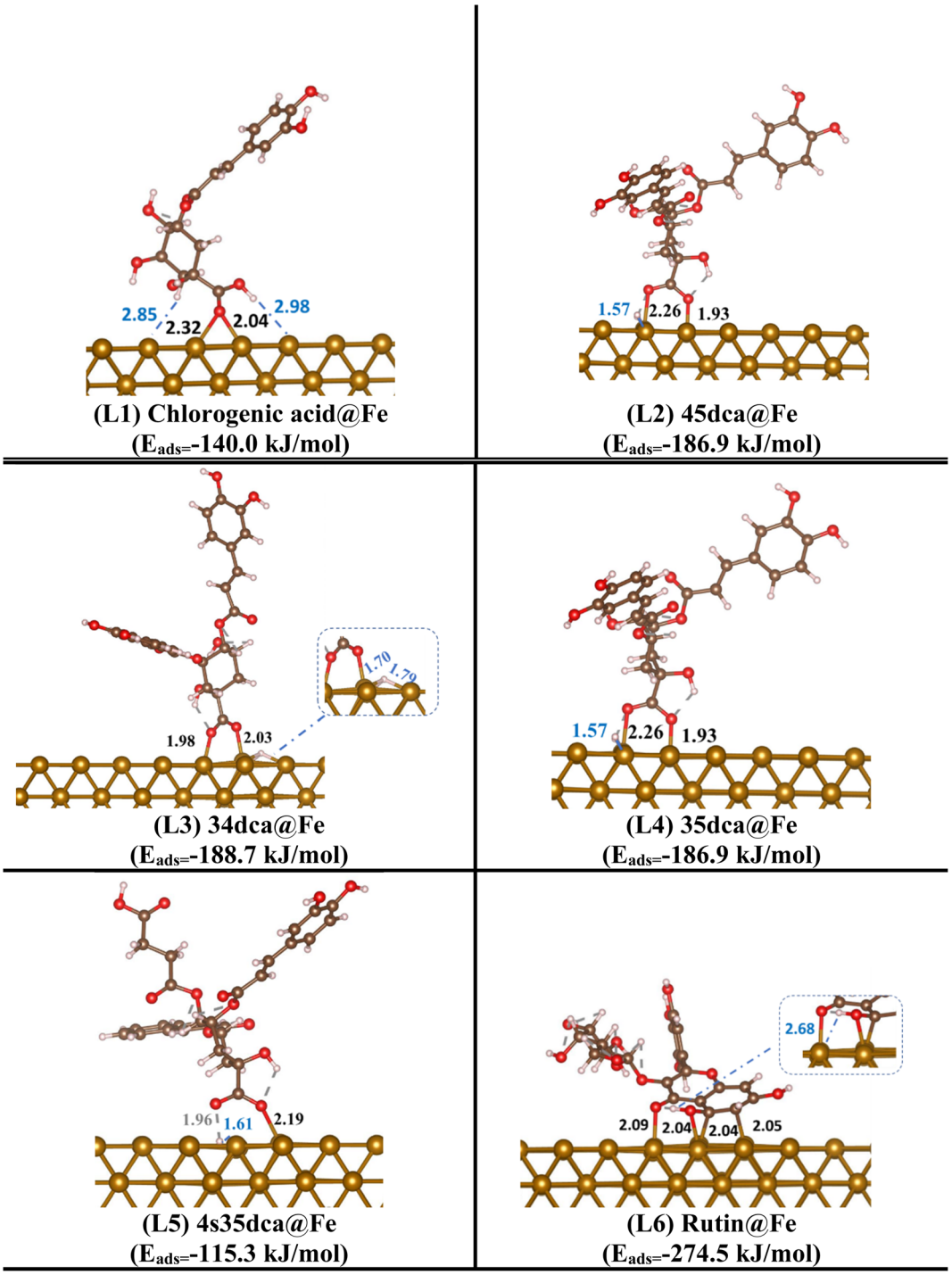

Fig. 17 The side view of optimized structures for the investigated inhibitors on the Fe (110) surface at the aqueous solution with their adsorption energies (E_{ads} in kJ mol^{-1}) and covalent bond lengths between Fe and C and O atoms (d_{Fe-C}, d_{Fe-O} in Å) in black font. The dashed blue and grey lines indicated non-classical hydrogen bonds ($d_{Fe\cdots H}$) and hydrogen bonding ($d_{O\cdots H}$), respectively. Code colure: Fe in light brown, O in red, C in dark brown, and H in white.

electrophilic attacks, while C47 and C45 show the maximum tendency for nucleophilic attacks. Finally, for the **L6** inhibitor, the atoms C31, O12, and C30 are the most favorable centers for nucleophilic attacks, while the atoms O16, C33, and C29 are the most favorable centers for nucleophilic attacks, see Fig. 16f and Table SD6.†

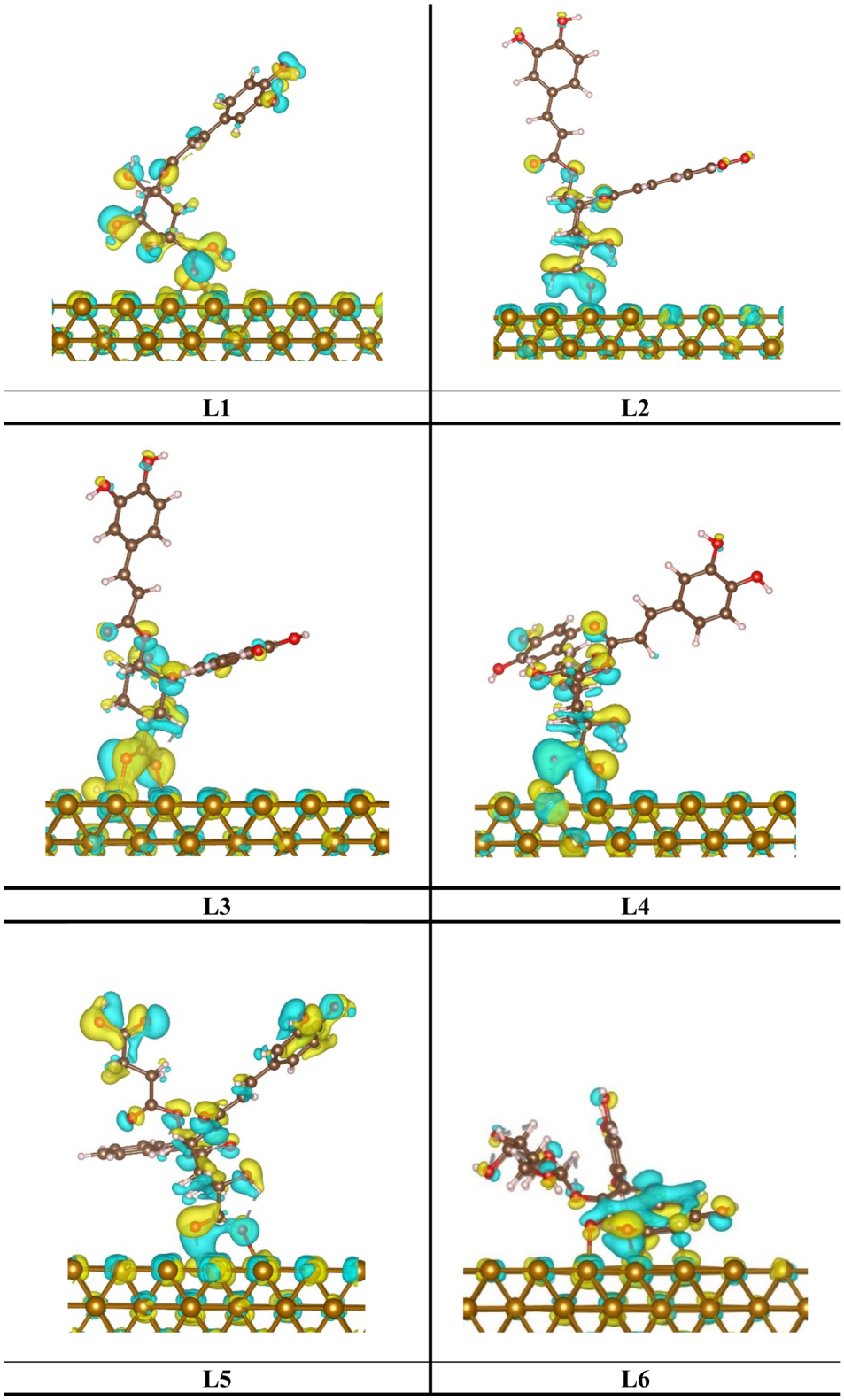

Fig. 18 CDD for the investigated inhibitors on the Fe surface at the aqueous solution. Note: the electron excess and deficit regions are represented with blue and yellow colors, respectively, and isosurfaces of 0.04 e bohr^{-3}.

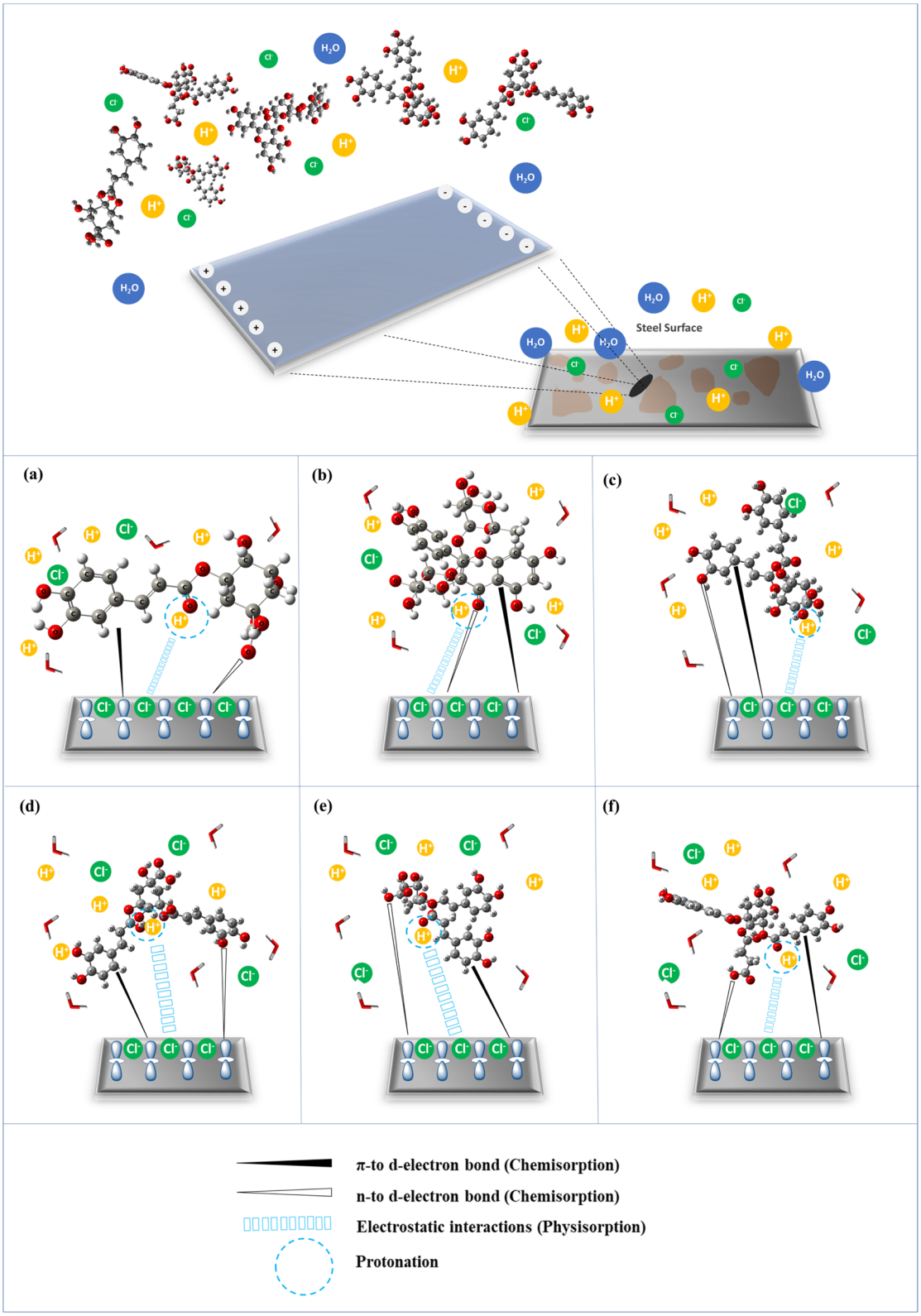

Fig. 19 The adsorption regime of the CCLE phytoconstituents towards the carbon steel active sites: (a) chlorogenic acid, (b) rutin, (c) 3,4 dicaffeoylquinic acid, (d) 3,5 dicaffeoylquinic acid, (e) 4,5 dicaffeoylquinic acid, (f) 4-succinyl-3,5-dicaffeoylquinic acid.

The above results indicate that the most favorable sites for electrophilic attacks, which are able to donate electrons to the unoccupied 3d-orbitals of Fe metal are the oxygen atoms and some carbon atoms, while the most favorable sites for nucleophilic attacks, which are responsible for accepting electrons from the occupied 3d-orbitals of the Fe-metal are the carbon atoms of the carbonyl groups.

3.9 Adsorption inhibitors on Fe (110)

To illustrate how the inhibitors interact with Fe (110) surface by PBE-D3, Fig. 17 depicts adsorption systems with their adsorption energies. Each inhibitor studied contains –C═O and –OH functional groups that are chemically bonded to the surface. According to the calculations, the process of forming bonds between Fe and inhibitors is exothermic. As well, all inhibitors exhibited negative adsorption energies between −108 and −275 kJ mol^{-1}.

Among all investigated systems, Rutin@Fe is the one that is strongly interaction with surface with adsorption energy of −274.50 kJ mol^{-1}. Due to multiple bonds with Fe surface. It is observed that adsorption energies have been increasing as **L6** (−274.5 kJ mol^{-1}) > **L3** (−188.5 kJ mol^{-1}) > **L4** (−186.9 kJ mol^{-1}) ≈ **L2** (−186.9 kJ mol^{-1}) > **L1** (−140.0 kJ mol^{-1}) > **L5** (−115.3 kJ mol^{-1}). Both 34dca and 35dca are binding with Fe surface by two –C═O and the hydrogen of hydroxyl groups is transferred to bond with Fe atoms. Those Fe–H bonds have bond lengths between 1.57 to 1.79 Å. On the other hand, the other systems Chlorogenic acid@Fe, Rutin@Fe, and 4s35dca@Fe formed one or two non-classical Fe–H bonds. Their bond lengths range between 2.98 to 1.61 Å, which is different from the standard (1.50 Å) about 1.48 to 0.11 Å. Several studies have demonstrated nonclassical interactions between the H atoms in inhibitors and the transition metal center.[99,100]

The interactions between the investigated inhibitor and with Fe surface can be further characterized using the charge density difference (CDD) tool, see Fig. 18. By using DFT calculations, this tool illustrates the redistribution of charge caused by chemical/physical bonds. Their idea is based on the change between the system of interest and its reference. All inhibitors cause an electron density deficit between the carbonyl groups and Fe and iron atoms, indicating that an O–Fe chemical bond is formed.

3.10 Suggested corrosion mechanism

When presented in an acidic environment, botanical-derived organic compounds, such as those found in the examined extract, provide a substantially more sustainable and enduring substitute to conventional corrosion inhibitors.[27,101] The compounds analyzed in this study, which are chlorogenic acid, rutin, 3,4-dicaffeoylquinic acid, 3,5-dicaffeoylquinic acid, 4,5-dicaffeoylquinic acid, and 4-succinyl-3,5-dicaffeoylquinic acid, exhibits structural features that facilitate chemisorption onto the steel surface, a key mechanism in corrosion inhibition. When exposed to a corrosive electrolyte, an electric charge accumulates at the interface, resulting in a positive charge on the metal surface.[102,103] Chemisorption occurs primarily through the interaction of the π–electrons of aromatic rings and the vacant d-orbitals of metallic iron, as well as through the donation of unshared electrons from oxygen atoms present in the phenolic, carboxylic, and glycosidic moieties of these compounds.[104] Fig. 19 illustrates these processes, showcasing the interplay of π–electron interactions, oxygen electron donation, and the formation of a cohesive adsorbed layer that enhances the corrosion resistance of the metal. The aromatic systems within chlorogenic acid and dicaffeoylquinic acids serve as electron-rich regions, with their delocalized π–electrons forming coordinate bonds with the positively charged steel surface. This interaction creates a stable adsorbed layer that minimizes the exposure of the steel to corrosive ions. The oxygen atoms in the hydroxyl (–OH) groups and carboxylic (–COOH) functionalities also play a significant role, with their lone pairs forming strong coordination bonds with the metal surface. For instance, the carboxylic groups in dicaffeoylquinic acids can deprotonate in acidic media, enhancing their electron-donating ability and facilitating direct bonding with the metallic substrate. Similarly, the multiple hydroxyl groups in rutin, combined with its conjugated aromatic rings, provide numerous active sites for chemisorption, resulting in a dense protective barrier. The bulky structure of 4-succinyl-3,5-dicaffeoylquinic acid, containing both caffeoyl and succinyl groups, further contributes to a compact and uniform organic layer that hinders the penetration of aggressive ions such as chloride.[105] This synergistic interaction, involving π–electrons, unshared oxygen electrons, and the surface d-orbitals, highlights the ability of the extract's compounds to form a robust chemisorbed layer, effectively reducing the corrosion rate of carbon steel in acidic conditions.

4 Conclusion

In conclusion, this study delved into the intricate mechanisms underlying the corrosion inhibition properties of *Chrysanthemum coronarium* leaf extract (CCLE) on carbon steel in acidic environments. Through a comprehensive investigation involving phytochemical analysis, spectroscopic techniques, electrochemical studies, and theoretical modeling, significant insights have been gained. The phytochemical analysis revealed the richness of CCLE in polyphenols and flavonoids, suggesting its potential as a corrosion inhibitor. This was corroborated by spectroscopic surface studies, which identified the formation of an organic-based protective layer on the steel surface through adsorption of the phytoconstituents from the *Chrysanthemum coronarium* leaves extract. Furthermore, electrochemical studies demonstrated that CCLE effectively reduces the corrosion rate of carbon steel in acidic media. This inhibition mechanism involves multiple interactive processes, including chemisorption processes, leading to the formation of a uniform adsorbed layer that hinders the ingress of corrosive ions onto the metal surface. Theoretical modeling using Density Functional Theory (DFT) and Molecular Dynamics (MD) simulations provided further insights into the molecular-level interactions between CCLE compounds and the steel surface, in which, the DFT method using B3LYP/6-31+G(d,p) in aqueous solution has been

used to study the anticorrosive performance of the of the components of the *Chrysanthemum coronarium* leaves extract. Analysis of the global chemical reactivity descriptors reveals that the 4-succinyl-3,5-dicaffeoylquinic acid (**L5**) component has the maximum corrosion inhibition efficiency, while rutin (**L6**) has the least contribution in the protection of the Fe-metal against corrosion. The analysis of local reactivity indices (Fukui indices) concludes that the oxygen atoms are able to interact with the Fe-metal by electron donation process, while the carbonyl carbon atoms have the ability to interact with the Fe-metal by electron acceptance process. Molecular dynamic (MD) simulation has been performed to calculate the adsorption energies of the inhibitors over the surface of the metal, highlighting the promising prospects of exploiting natural plant extracts, such as *Chrysanthemum coronarium* leaves extract, as effective corrosion inhibitors, paving the way for sustainable solutions in corrosion control and mitigation.

Data availability

The data supporting this article have been included as part of the ESI.†

Conflicts of interest

The authors declare that they have no known competing financial interests or personal relationships that could have appeared to influence the work reported in this paper.

Acknowledgements

The authors gratefully acknowledge the High-Performance Computing Centre (Aziz Supercomputer) at King Abdulaziz University (**http://hpc.kau.edu.sa**) for assisting with the calculations for this study. This project was funded by the Deanship of Scientific Research (DSR), King Abdulaziz University, Jeddah, under grant no. (GPIP-732-247-2024); the authors, therefore, gratefully acknowledge DSR's technical and financial support. The authors would like to thank the National Center for Scientific and Technical Research (CNRST) of Morocco for putting at their disposal the technical facilities of the UATRS division.

References

1 IndustryARC, Corrosion Monitoring Market – Forecast (2024–2030).
2 G. Koch, J. Varney, N. Thompson, O. Moghissi, M. Gould and J. Payer, *NACE Int.*, 2016, 1–216.
3 S. H. Alrefaee, K. Y. Rhee, C. Verma, M. A. Quraishi and E. E. Ebenso, *J. Mol. Liq.*, 2021, **321**, 114666.
4 R. Aslam, G. Serdaroglu, S. Zehra, D. Kumar Verma, J. Aslam, L. Guo, C. Verma, E. E. Ebenso and M. A. Quraishi, *J. Mol. Liq.*, 2022, **348**, 118373.
5 Q. H. Zhang, N. Xu, Z. N. Jiang, H. F. Liu and G. A. Zhang, *J. Colloid Interface Sci.*, 2023, **640**, 1052–1067.
6 C. Verma, E. E. Ebenso, M. A. Quraishi and C. M. Hussain, *Mater. Adv.*, 2021, **2**, 3806–3850.
7 Q. Wang, Q. Zhang, H. Zheng, L. Liu, X. Wu, C. Zhao, X. Zhou, Y. Sun, Z. Yan and X. Li, *Sustainable Chem. Pharm.*, 2023, **34**, 101177.
8 M. Akbari Shahmirzadi and M. Azadi, *Heliyon*, 2024, **10**, e29962.
9 T. Rajachandrasekar, I. Muthuvel, K. Kavitha, S. R. Anishia, S. Sasikruba and S. Sujatha, *Mater. Today: Proc.*, 2024, DOI: **10.1016/j.matpr.2024.04.024**.
10 B. Lin, X. Zhou, T. Duan, C. Zhao, J. Zhu and Y. Xu, *Arabian J. Chem.*, 2024, **17**, 105410.
11 D. I. Udunwa, O. D. Onukwuli, M. C. Menkiti, S. C. Nwanonenyi, C. B. Ezekannagha and C. O. Aniagor, *J. Mol. Struct.*, 2024, **1302**, 137508.
12 G. D. Pai, M. R. Rathod, R. S K and A. A. Kittur, *Results Surf. Interfaces*, 2024, **15**, 100203.
13 A. Kumar and C. Das, *Sci. Total Environ.*, 2024, **929**, 172569.
14 F.-Z. Eddahhaoui, A. Najem, M. Elhawary, M. Boudalia, O. S. Campos, M. Tabyaoui, A. José Garcia, A. Bellaouchou and H. M. A. Amin, *J. Alloys Compd.*, 2024, **977**, 173307.
15 Q. Wang, C. Zhao, R. Wang, R. Aslam, X. Zhou, Q. Zhang, Z. Yan, Y. Sun, X. Li and H. Zheng, *Colloids Surf., A*, 2024, **682**, 132904.
16 B. Tan, Y. Liu, Z. Gong, X. Zhang, J. Chen, L. Guo, J. Xiong, J. Liu, R. Marzouki and W. Li, *J. Mol. Liq.*, 2024, **397**, 124117.
17 R. Kellal, D. Benmessaoud Left, Z. S. Safi, N. Wazzan, O. S. Al-Qurashi and M. Zertoubi, *J. Ind. Eng. Chem.*, 2023, **125**, 370–389.
18 O. Dagdag, Z. Safi, H. Erramli, N. Wazzan, I. B. Obot, E. D. Akpan, C. Verma, E. E. Ebenso, O. Hamed and A. El Harfi, *J. Mol. Liq.*, 2019, **287**, 110977.
19 M. Tang, X. Li, S. Deng and R. Lei, *J. Mol. Liq.*, 2021, **344**, 117926.
20 Ecocrop, *Chrysanthemum coronarium Var. Coronarium*, Rome,Italie., 2007.
21 N. Hossain, M. Aminul Islam and M. Asaduzzaman Chowdhury, *Results Chem.*, 2023, **5**, 100883.
22 K. Hosni, I. Hassen, H. Sebei and H. Casabianca, *Ind. Crops Prod.*, 2013, **44**, 263–271.
23 L. Sulas, G. L. Petretto, G. Pintore and G. Piluzza, *Nat. Prod. Res.*, 2017, **31**, 2941–2944.
24 J. P. Lai, Y. H. Lim, J. Su, H. M. Shen and C. N. Ong, *J. Chromatogr. B:Anal. Technol. Biomed. Life Sci.*, 2007, **848**, 215–225.
25 Y. Chuda, H. Ono, M. Ohnishi-Kameyama, T. Nagata and T. Tsushida, *J. Agric. Food Chem.*, 1996, **44**, 2037–2039.
26 T. Murayama, H. Yada, M. Kobori, H. Shinmoto and T. Tsushida, *J. Jpn. Soc. Hortic. Sci.*, 2002, **71**, 236–242.
27 Z. Ait EL Caid, D. Benmessaoud Left, R. Kellal, Z. S. Safi, A. Thoume, N. A. Wazzan and M. Zertoubi, *Mater. Chem. Phys.*, 2024, **316**, 129081.
28 B. lan Lin, T. hu Duan and Y. ye Xu, *J. Mol. Struct.*, 2024, DOI: **10.1016/j.molstruc.2024.140351**.
29 Z. Jebali, H. Ferkous, M. Zerroug, A. Boublia, A. Delimi, A. Bouzid, H. Majdoub, B. Ernst, N. Elboughdiri and Y. Benguerba, *J. Environ. Chem. Eng.*, 2024, **12**, 112374.

30 A. Ehsani, M. G. Mahjani, M. Hosseini, R. Safari, R. Moshrefi and H. Mohammad Shiri, *J. Colloid Interface Sci.*, 2017, **490**, 444–451.
31 J. Dai and X. An, *Int. J. Electrochem. Sci.*, 2023, **18**, 100080.
32 B. Cherinka, B. H. Andrews, J. Sánchez-Gallego, J. Brownstein, M. Argudo-Fernández, M. Blanton, K. Bundy, A. Jones, K. Masters and D. R. Law, *Astron. J.*, 2019, **158**, 74.
33 D. Roy, T. A. Keith, and J. M. Millam, *Current version: GaussView, version 6*, Semichem Inc., 2016.
34 R. A., *Gaussian09*, Inc., Wallingford CT, 2009, vol. 121, pp. 150–166.
35 A. D. Becke, *Phys. Rev. A*, 1988, **38**, 3098.
36 A. D. Becke, *J. Chem. Phys.*, 1996, **104**, 1040–1046.
37 C. Lee, W. Yang and R. G. Parr, *Phys. Rev. B: Condens. Matter Mater. Phys.*, 1988, **37**, 785–789.
38 Ş. Erdoğan, Z. S. Safi, S. Kaya, D. Ö. Işın, L. Guo and C. Kaya, *J. Mol. Struct.*, 2017, **1134**, 751–761.
39 Z. S. Safi and A. M. Lamsabhi, *J. Phys. Org. Chem.*, 2010, **23**, 751–758.
40 R. Hsissou, K. Dahmani, A. El Magri, A. Hmada, Z. Safi, N. Dkhireche, M. Galai, N. Wazzan and A. Berisha, *Polymers*, 2023, **15**, 1967.
41 B. Mennucci, J. Tomasi, R. Cammi, J. R. Cheeseman, M. J. Frisch, F. J. Devlin, S. Gabriel and P. J. Stephens, *J. Phys. Chem. A*, 2002, **106**, 6102–6113.
42 A. E. Reed, R. B. Weinstock and F. Weinhold, *J. Chem. Phys.*, 1985, **83**, 735–746.
43 S. H. Kouadri I, *Ind. Crops Prod.*, 2018, **124**, 787–796.
44 I. Kouadri, A. Layachi, A. Makhlouf and H. Satha, *Int. J. Polym. Anal. Charact.*, 2018, **23**, 362–375.
45 V. S. Sastri and J. R. Perumareddi, *Corrosion*, 1997, **53**, 617–622.
46 R. G. Parr and R. G. Pearson, *J. Am. Chem. Soc.*, 1983, **105**, 7512–7516.
47 R. G. Parr, L. v Szentpály and S. Liu, *J. Am. Chem. Soc.*, 1999, **121**, 1922–1924.
48 R. G. Pearson, *J. Am. Chem. Soc.*, 1963, **85**, 3533–3539.
49 W. Yang and R. G. Parr, *Proc. Natl. Acad. Sci. U. S. A.*, 1985, **82**, 6723–6726.
50 T. Koopmans, *Physica*, 1933, **1**, 104–113.
51 L. Guo, Z. S. Safi, S. Kaya, W. Shi, B. Tüzün, N. Altunay and C. Kaya, *Front. Chem.*, 2018, **6**, 155.
52 B. Gómez, N. V. Likhanova, M. A. Domínguez-Aguilar, R. Martínez-Palou, A. Vela and J. L. Gázquez, *J. Phys. Chem. B*, 2006, **110**, 8928–8934.
53 K. Fukui, T. Yonezawa and H. Shingu, *J. Chem. Phys.*, 1952, **20**, 722–725.
54 A. K. Chandra and M. T. Nguyen, in *Chemical Reactivity Theory: A Density-Functional View*, ed. P. K. Chattaraj, Taylor and Francis, New York, 2008.
55 J. Hafner and G. Kresse, The Vienna AB-Initio Simulation Program VASP: An Efficient and Versatile Tool for Studying the Structural, Dynamic, and Electronic Properties of Materials, in *Properties of Complex Inorganic Solids*, ed. A. Gonis, A. Meike, P. E. A. Turchi, 1997, Springer, Boston, MA, DOI: 10.1007/978-1-4615-5943-6_10.
56 M. Hao, W. Zeng and Y. Li, *Phys. E*, 2022, **135**, 114938.
57 L. Xu, D. Kirvassilis, Y. Bai and M. Mavrikakis, *Surf. Sci.*, 2018, **667**, 54–65.
58 H. J. Monkhorst and J. D. Pack, *Phys. Rev. B*, 1976, **13**, 5188–5192.
59 S. Grimme, S. Ehrlich and L. Goerigk, *J. Comput. Chem.*, 2011, **32**, 1456–1465.
60 K. Mathew, R. Sundararaman, K. Letchworth-Weaver, T. A. Arias and R. G. Hennig, *J. Chem. Phys.*, 2014, **140**, 84106.
61 V. Vorobyova and M. Skiba, *Waste Biomass Valorization*, 2021, **12**, 4623–4641.
62 A. Thakur, S. Kaya, A. S. Abousalem, S. Sharma, R. Ganjoo, H. Assad and A. Kumar, *Process Saf. Environ. Prot.*, 2022, **161**, 801–818.
63 H. Yang, S. Deng and X. Li, *Int. J. Electrochem. Sci.*, 2024, **19**, 100790.
64 B. Tamilselvi, D. S. Bhuvaneshwari, S. Padmavathy and P. B. Raja, *J. Mol. Liq.*, 2022, **359**, 119359.
65 Z. Shahryari and K. Gheisari, *Mater. Chem. Phys.*, 2023, **299**, 127474.
66 A. Batah, A. Chaouiki, O. I. El Mouden, M. Belkhaouda, L. Bammou and R. Salghi, *Sustainable Chem. Pharm.*, 2022, **27**, 100677.
67 R. H. Ellerbrock and H. H. Gerke, *J. Plant Nutr. Soil Sci.*, 2021, **184**, 388–397.
68 M. Iranpour, A. Babaei and M. Bagherzadeh, *Results Surf. Interfaces*, 2023, **13**, 100163.
69 H. Mobtaker, M. Azadi and M. Rassouli, *Heliyon*, 2022, **8**, e12297.
70 A. Berrissoul, A. Ouarhach, F. Benhiba, A. Romane, A. Guenbour, B. Dikici and F. Bentiss, *Ind. Crops Prod.*, 2022, **187**, 115310.
71 Z. Ait El Caid, D. Benmessaoud Left, A. Thoume, R. Kellal and M. Zertoubi, *J. Bio- Tribo-Corros.*, 2024, **10**, 9.
72 M. Errami, A. EL-Asri, S. Fdil, S. Ourouadi, O. Iddelmouiden, A. Jmiai, L. Bazzi, A. Hadfi and R. Ait Akbour, *Colloids Surf., A*, 2024, **689**, 133684.
73 R. Kellal, D. Benmessaoud Left, M. Azzi and M. Zertoubi, *J. Appl. Electrochem.*, 2023, **53**, 811–832.
74 Z. Ait El Caid, D. Benmessaoud Left, A. Thoume, R. Kellal and M. Zertoubi, *J. Bio- Tribo-Corros.*, 2023, **9**, 83.
75 M. Faustin, *Etude de l'effet des alcaloïdes sur la corrosion de l'acier C38 en milieu acide chlorhydrique 1M : Application à Aspidosperma album et Geissospermum laeve (Apocynacées)*, Université des Antilles et de la Guyane, 2013.
76 H. Khoshsang and A. Ghaffarinejad, *Chem. Data Collect.*, 2022, **37**, 100799.
77 B. Fan, X. Zhao, Z. Liu, Y. Xiang and X. Zheng, *Sustainable Chem. Pharm.*, 2022, **29**, 100821.
78 G. K. Shamnamol, P. Rugma, S. John and J. Mary Jacob, *Results Chem.*, 2023, **5**, 100728.
79 R. Tolulope Loto, *Mater. Today: Proc.*, 2023, **80**, 1519–1524.
80 A. Kumar and C. Das, *Sustainable Chem. Pharm.*, 2023, **36**, 101261.
81 X. Liu, Y. Gao, J. Guan, Q. Zhang, Y. Lin, C. Shi, Y. Wang, J. Du and N. Ma, *Arabian J. Chem.*, 2023, **16**, 105066.

82 R. Kellal, D. Benmessaoud Left, Z. S. Safi, A. Thoume, N. A. Wazzan, O. S. AL-Qurashi and M. Zertoubi, *Mater. Chem. Phys.*, 2024, **314**, 128846.
83 M. Faustin, A. Maciuk, P. Salvin, C. Roos and M. Lebrini, *Corros. Sci.*, 2015, **92**, 287–300.
84 J. P. P. Thanikaivelan, V. Subramanian and T. Ramasami, *Theor. Chem. Acc.*, 2002, **107**, 326–335.
85 N. O. Obi-Egbedi, I. B. Obot and S. A. Umoren, *Arabian J. Chem.*, 2012, **5**, 361–373.
86 R. González Gómez, I. del Rosal, K. Philippot and R. Poteau, *Theor. Chem. Acc.*, 2019, **138**, 1–10.
87 S. Martinez, *Mater. Chem. Phys.*, 2003, **77**, 97–102.
88 M. J. S. Dewar and W. Thiel, *J. Am. Chem. Soc.*, 1977, **99**, 4899–4907.
89 A. Kokalj, *Chem. Phys.*, 2012, **393**, 1–12.
90 H. Babas, M. Khachani, I. Warad, S. Ajebli, A. Guessous, A. Guenbour, Z. Safi, A. Berisha, A. Bellaouchou and Z. Abdelkader, *J. Mol. Liq.*, 2022, **356**, 119019.
91 I. Lukovits, K. Palfi, I. Bako and E. Kalman, *Corrosion*, 1997, **53**, 915–919.
92 I. Lukovits, E. Kálmán and F. Zucchi, *Corrosion*, 2001, **57**, 3–8.
93 P. Geerlings, F. De Proft and W. Langenaeker, *Chem. Rev.*, 2003, **103**, 1793–1874.
94 S.-B. Liu, *Acta Phys.-Chim. Sin.*, 2009, **25**, 590–600.
95 T. Lu and F. Chen, *J. Comput. Chem.*, 2012, **33**, 580–592.
96 A. D. S. K. Saha, P. Ghosh, D. Sukul and P. Banerjee, *Phys. Chem. Chem. Phys.*, 2016, **18**, 17898–17911.
97 C. Morell, A. Grand and A. Toro-Labbé, *J. Phys. Chem. A*, 2005, **109**, 205–212.
98 C. Cárdenas, N. Rabi, P. W. Ayers, C. Morell, P. Jaramillo and P. Fuentealba, *J. Phys. Chem. A*, 2009, **113**, 8660–8667.
99 H. Hashimoto, T. Fukuda, H. Tobita, M. Ray and S. Sakaki, *Angew. Chem., Int. Ed.*, 2012, **51**, 2930–2933.
100 M. Ray, Y. Nakao, H. Sato, S. Sakaki, T. Watanabe, H. Hashimoto and H. Tobita, *Organometallics*, 2010, **29**, 6267–6281.
101 R. Kellal, Z. Ait El Caid, A. Thoume, M. Zertoubi and D. Benmessaoud Left, *J. Bio- Tribo-Corros.*, 2024, **10**, 69.
102 Z. A. El Caid, D. Benmessaoud Left and M. Zertoubi, *J. Mol. Struct.*, 2024, **1300**, 137218.
103 A. Thoume, D. Benmessaoud Left, A. Elmakssoudi, Z. S. Safi, N. Benzbiria, A. Berisha, R. Kellal and M. Zertoubi, *Mater. Chem. Phys.*, 2023, **310**, 128487.
104 L. Chahir, M. El Faydy, N. Abad, F. Benhiba, I. Warad, D. Benmessaoud Left, M. Zertoubi, M. Allali, G. Kaichouh, B. Dikici, A. Bellaouchou, Y. Ramli and A. Zarrouk, *J. Bio- Tribo-Corros.*, 2024, **10**, 36.
105 Z. A. El Caid, D. B. Left, A. Thoume, R. Kellal and M. Zertoubi, *J. Bio- Tribo-Corros.*, 2023, **9**, 83.